Integration of MODIS land and atmosphere products with a coupled-process model to estimate gross primary productivity and evapotranspiration from 1 km to global scales

Youngryel Ryu,[1,2] Dennis D. Baldocchi,[1] Hideki Kobayashi,[1] Catharine van Ingen,[3] Jie Li,[4] T. Andy Black,[5] Jason Beringer,[6] Eva van Gorsel,[7] Alexander Knohl,[8] Beverly E. Law,[9] and Olivier Roupsard[10,11]

Received 11 February 2011; revised 3 September 2011; accepted 23 October 2011; published 30 December 2011.

[1] We propose the Breathing Earth System Simulator (BESS), an upscaling approach to quantify global gross primary productivity and evapotranspiration using MODIS with a spatial resolution of 1–5 km and a temporal resolution of 8 days. This effort is novel because it is the first system that harmonizes and utilizes MODIS Atmosphere and Land products on the same projection and spatial resolution over the global land. This enabled us to use the MODIS Atmosphere products to calculate atmospheric radiative transfer for visual and near infrared radiation wave bands. Then we coupled atmospheric and canopy radiative transfer processes, with models that computed leaf photosynthesis, stomatal conductance and transpiration on the sunlit and shaded portions of the vegetation and soil. At the annual time step, the mass and energy fluxes derived from BESS showed strong linear relations with measurements of solar irradiance (r^2 = 0.95, relative bias: 8%), gross primary productivity (r^2 = 0.86, relative bias: 5%) and evapotranspiration (r^2 = 0.86, relative bias: 15%) in data from 33 flux towers that cover seven plant functional types across arctic to tropical climatic zones. A sensitivity analysis revealed that the gross primary productivity and evapotranspiration computed in BESS were most sensitive to leaf area index and solar irradiance, respectively. We quantified the mean global terrestrial estimates of gross primary productivity and evapotranpiration between 2001 and 2003 as 118 ± 26 PgC yr^{-1} and 500 ± 104 mm yr^{-1} (equivalent to 63,000 ± 13,100 km^3 yr^{-1}), respectively. BESS-derived gross primary productivity and evapotranspiration estimates were consistent with the estimates from independent machine-learning, data-driven products, but the process-oriented structure has the advantage of diagnosing sensitivity of mechanisms. The process-based BESS is able to offer gridded biophysical variables everywhere from local to the total global land scales with an 8-day interval over multiple years.

Citation: Ryu, Y., et al. (2011), Integration of MODIS land and atmosphere products with a coupled-process model to estimate gross primary productivity and evapotranspiration from 1 km to global scales, *Global Biogeochem. Cycles*, *25*, GB4017, doi:10.1029/2011GB004053.

1. Introduction

[2] There is great interest and need to estimate terrestrial trace gas and energy fluxes (e.g., CO_2 and water) everywhere (e.g., local to the global land) and all the time (e.g., 8-daily over multiple years). There have been recent advances to produce such estimates by using machine-learning techniques in conjunction with remote sensing data and the flux tower data derived from sparse networks [*Beer et al.*, 2010; *Jung et al.*, 2010; *Xiao et al.*, 2010]. However, the

[1]Department of Environmental Science, Policy and Management, University of California, Berkeley, California, USA.
[2]Now at Department of Landscape Architecture and Rural Systems Engineering, Seoul National University, Seoul, South Korea.
[3]eScience Group, Microsoft Research, San Francisco, California, USA.
[4]Department of Computer Science, University of Virginia, Charlottesville, Virginia, USA.
[5]Faculty of Land and Food Systems, University of British Columbia, Vancouver, British Columbia, Canada.
[6]School of Geography and Environmental Science, Monash University, Melbourne, Victoria, Australia.
[7]CSIRO Marine and Atmospheric Research, Canberra, ACT, Australia.
[8]Chair of Bioclimatology, Büsgen Institute, Georg-August University of Göttingen, Göttingen, Germany.
[9]Department of Forest Ecosystems and Society, Oregon State University, Corvallis, Oregon, USA.
[10]CIRAD, UMR Ecologie Fonctionnelle and Biogéochimie des Sols and Agroécosystèmes, SupAgro-CIRAD-INRA-IRD, Montpellier, France.
[11]Centro Agronómico Tropical de Investigación y Enseñanza, Turrialba, Costa Rica.

0886-6236/11/2011GB004053

machine-learning technique relies on empirical relationships between forcing variables and fluxes [*Jung et al.*, 2009], and it only works within the domain of data on which it is trained.

[3] A process-based diagnostic model that is calibration-free and can be applied globally has the advantage of explaining the response of ecosystem metabolism to global change. This task requires understanding and quantifying a set of coupled and highly nonlinear biophysical processes that span 14 orders of magnitude in time and space [*Jarvis*, 1995; *Osmond et al.*, 1980]. While a generation ago, such an approach was discouraged due to concerns about the issue of "garbage-in and garbage-out" [*de Wit*, 1970]. Today, advancements in remote sensing, micrometeorology and ecophysiology together with some recent meta-analysis studies enable us to deduce key parameters and generate input variables to quantify mass and energy fluxes at high spatial and temporal resolution and across vast spatial and temporal scales.

[4] The key processes that are essential to quantify trace gas and energy fluxes have been identified. First, photosynthesis and transpiration needs to be coupled as they constrain each other via the stomata [*Baldocchi*, 1997; *Baldocchi and Meyers*, 1998; *Collatz et al.*, 1991; *Leuning et al.*, 1995]. Second, a two-leaf model (i.e., sunlit and shaded leaves) is more effective than a big leaf model; it is needed to consider nonlinear processes in canopy radiative transfer and trace gas fluxes [*Chen et al.*, 1999; *Dai et al.*, 2004; *de Pury and Farquhar*, 1997; *Norman*, 1982; *Sinclair et al.*, 1976; *Wang and Leuning*, 1998]. Third, foliar clumping effects should be considered as they influence canopy radiative transfer [*Norman and Jarvis*, 1975; *Ryu et al.*, 2010a, 2010b], change the proportion of sunlit and shade leaves, and consequently modify canopy fluxes [*Baldocchi and Wilson*, 2001; *Baldocchi et al.*, 1984; *Chen et al.*, 1999; *Lemeur and Blad*, 1974]. Fourth, atmospheric and land processes should be coupled as the environment of incoming shortwave radiation (e.g., the amount of diffuse radiation, solar zenith angle) substantially modulates surface reflectance and canopy processes [*Alton et al.*, 2007; *Gu et al.*, 2002; *Kobayashi and Iwabuchi*, 2008; *Ryu et al.*, 2010c].

[5] Most land surface flux models that use satellite-derived parameters and variables have not yet incorporated those processes. Typically, gross primary productivity (GPP) has been estimated using light use efficiency models [*Hilker et al.*, 2009; *Ruimy et al.*, 1996; *Running et al.*, 2004] or vegetation indices [*Huete et al.*, 2008; *Sims et al.*, 2008]. Evapotranspiration (ET) has been inferred from the energy balance residual [*Norman et al.*, 1995; *Su*, 2002], the Priestley-Taylor equation [*Fisher et al.*, 2008; *Priestley and Taylor*, 1972], the Penman-Monteith equation [*Cleugh et al.*, 2007; *Monteith*, 1965; *Mu et al.*, 2007] or the hydrological balance [*Rodell et al.*, 2004]. More recently, a statistical approach using machine-learning techniques has emerged as a new tool to quantify GPP and ET [*Beer et al.*, 2010; *Jung et al.*, 2009; *Xiao et al.*, 2010]. However, even fewer studies have attempted to connect GPP and ET in concert, at global scales [*Yuan et al.*, 2010]. Furthermore, many global models used data inputs and parameters from a mixture of fine (1 km) and coarse (0.5 to 1 degree) space scales. For example land surface properties like leaf area index (LAI), vegetation indices, and land surface temperature were derived with ~1 km resolution. In contrast, many models derived incoming solar irradiance, the most important driver of biophysical processes, and meteorological variables from coarse reanalysis data such as 1-degree resolution of DAO [*Zhao et al.*, 2005] and ISLSCP-II [*Fisher et al.*, 2008], 0.5-degree resolution of MERRA [*Yuan et al.*, 2010], and 0.125-degree resolution of NLDAS [*McCabe et al.*, 2008]. Thus it is important to recognize that there is a scale mismatch between land surface and atmospheric inputs that remains a challenge.

[6] Recent advances in remote sensing, ecophysiology and recent meta-analysis offer new opportunities to incorporate the key processes mentioned above into remote-sensing-based land surface models. The tight correlation between albedo and nitrogen concentration at closed canopy in temperate and boreal forests [*Hollinger et al.*, 2010; *Ollinger et al.*, 2008] enables us to apply Farquhar's photosynthesis model at coarse spatial scales using remote sensing. Several studies have demonstrated that MODIS atmospheric products can provide solar irradiance and meteorological variables at high spatial resolution (1–5 km) [*Liang et al.*, 2006; *Ryu et al.*, 2008a; *Van Laake and Sanchez-Azofeifa*, 2004], which provides a possibility to couple land surface and atmospheric processes at high spatial resolution. Next, a global scale foliar clumping index map by using multiangle satellite images has been developed and tested [*Chen et al.*, 2005; *Pisek et al.*, 2010]. Thus accurate calculation of canopy radiative transfer that is important in controlling GPP and ET has become possible by integrating incoming solar irradiance, LAI and clumping index information.

[7] In spite of the recent advances mentioned above, one important barrier to global scale remote sensing research remains. That is the computational resource and data storage. Global scale remote sensing study requires handling terabytes of data, in particular when targeting high spatial resolution (e.g., 1–5 km). Many environmental scientists do not have access to a high-performance computing to overcome such computational barriers. Recently, as an alternative, the cloud computing service (e.g., Microsoft Azure, Amazon EC2), a kind of web-based super computer, was used to perform these intensive time-demanding computations [*Li et al.*, 2010]. Also, corporate collaborations with scientists have opened doors for global analysis. For example, a significant advance is that Landsat satellite imagery from the last 25 years (much of which was not previously available online) made available by U.S. Geological Survey has been processed by the Google Earth Engine using an analytical tool [*Asner et al.*, 2005], which will allow fine-scale mapping of deforestation and forest degradation globally (http://earthengine.googlelabs.com).

[8] In this study, we present the Breathing Earth System Simulator (BESS) built on the Microsoft Azure cloud computing service. BESS couples algorithms and models that compute atmospheric radiative transfer, photosynthesis, and leaf and soil energy balances by integrating a range of data streams in MODIS atmospheric and land products with ancillary data. Together, this system can produce computations of canopy evaporation and photosynthesis from 1- to 5-km resolution across the globe at an 8-day time interval.

[9] The goals of this paper are: first, we describe the BESS algorithms. Then we evaluate the computational products of

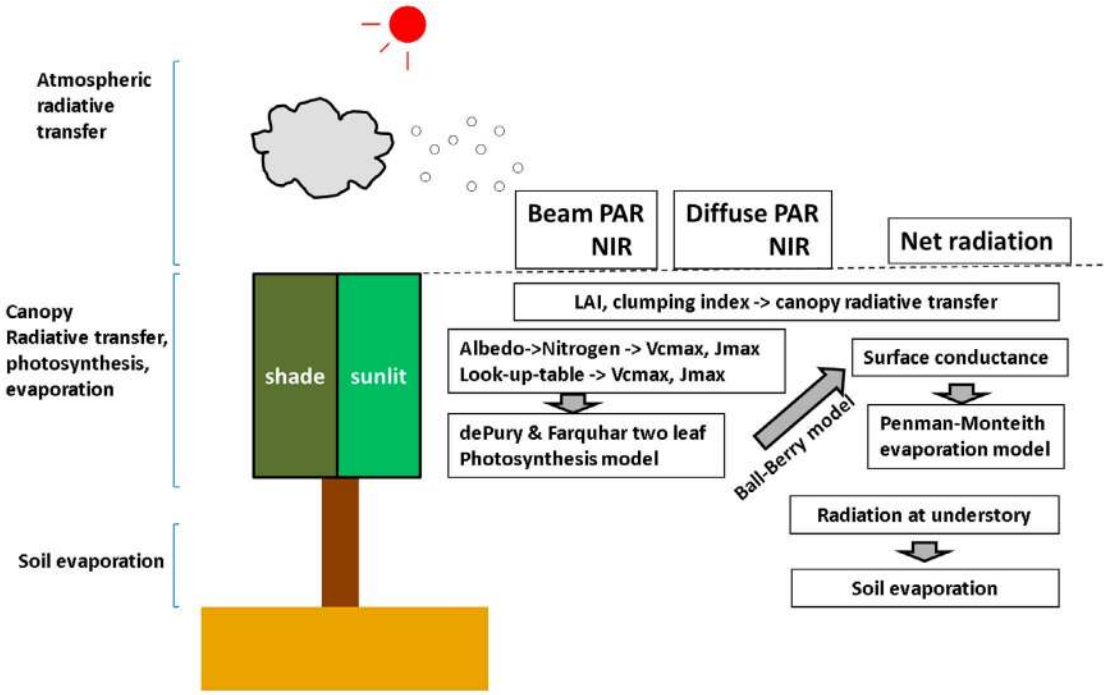

Figure 1. Overview of the coupled biophysical model (BESS).

BESS against 1) data from 33 flux towers across 7 plant functional types spanning arctic to tropical climatic zones, 2) data-driven GPP and ET products, and 3) basin scale water balance data. Last, we use BESS system to address several key scientific questions that include: 1) can BESS that does not explicitly consider soil water balance estimate GPP and ET reliably? 2) what are the global terrestrial estimates of GPP and ET at annual time scales? 3) how sensitive is BESS model to environmental and biological drivers?

2. Methods

2.1. BESS Description

[10] BESS is a biophysical model (Figure 1). In this section, we describe coupled the key modules that include: atmospheric radiative transfer (section 2.1.1), canopy radiative transfer (section 2.1.2), canopy photosynthesis (section 2.1.3), maximum carboxylation rate (section 2.1.4), two-leaf canopy conductance and temperature (section 2.1.5), and evapotranspiration (section 2.1.6), which are important to drive this process based approach.

2.1.1. Atmospheric Radiative Transfer Model

[11] To calculate incoming shortwave radiation ($R_{s,i}$, see nomenclature in Appendix A), photosynthetic active radiation ($R_{p,i}$) and near-infrared radiation ($R_{n,i}$) for the beam and diffuse components at the top of canopy, we used an atmospheric radiative transfer model (FLiES) based on the Monte-Carlo approach [*Iwabuchi*, 2006; *Kobayashi and Iwabuchi*, 2008]. This model was compared with two other atmospheric radiative transfer models, 6S model [*Vermote et al.*, 1997] and Streamer V3.0 [*Key and Schweiger*, 1998], and they showed good agreement among each other. The relative RMSE was 4.3% and 6.7%, for between the current model and 6S model, and for between the current model and Streamer V3.0, respectively across a range of atmospheric condition [*Kobayashi and Iwabuchi*, 2008]. To apply the atmospheric radiative transfer model to the globe and reduce computational needs, we developed a look-up-table for each radiation component. The input variables include: 1) solar zenith angle (5, 10, …, 85°), 2) aerosol optical thickness at 550 nm (0.1, 0.3, 0.5, 0.7, 0.9), 3) cloud optical thickness (0.1, 0.5, 1, 5, 10, 20, 40, 60, 80, 110), land surface albedo (0.1, 0.4, 0.7), 4) cloud top height (1000, 3000, 5000, 7000, 9000 m), 5) atmospheric profile type (tropical zone for Tropical type, arid and temperate zones for Midlatitude type, snow and ice zones for High-latitude type; the climate zones were defined by Köppen-Geiger global climate classification map (see section 2.4.4), the atmospheric profile was characterized by *Hess et al.* [1998]), 6) aerosol type (continental average except for tropical climatic zone whose aerosol type was assigned as urban to consider high aerosol loading in tropics [*Martin et al.*, 2010], the aerosol type was characterized by *Hess et al.* [1998]), and 7) cloud type (cloud-free, stratus continental, cumulous continental) [*Hess et al.*, 1998]. We prepared the input data from a range of MODIS data streams including MOD04 (aerosol optical thickness), MOD06 (solar zenith angle, cloud optical thickness, cloud top height), and MCD43 (albedo). As MODIS did not provide the types of aerosol and cloud, we used two categories for aerosol (continental average and urban), and applied two categories for cloud type (stratus continental and cumulous continental). We used the cumulous continental type for the tropical climate zone (see section 2.4.4), and the stratus continental type for the other areas. The sensitivity analysis revealed that different cloud and aerosol type combinations could lead to a maximum difference of 10% and 15%, respectively in the incoming Q_P calculation (data not shown).

2.1.2. Two-Leaf Canopy Radiative Transfer Model

[12] We applied a simple canopy radiative transfer model that quantified absorbed photosynthetically active radiation (PAR), near-infrared radiation (NIR) and longwave radiation for sunlit and shade leaves. The sunfleck penetration (f_{sun}), the probability of leaf area being irradiated by the direct beam, plays a key role in the model. The sunlit and shaded leaves receive different amounts of radiation thus the expected value of canopy fluxes should be weighted by the fractions of sunlit and shade leaves to consider nonlinear processes in the canopy fluxes. *Gutschick* [1991] derived f_{sun} at canopy depth L for clumped canopy:

$$f_{sun}(L) = \frac{\exp(-kL\Omega) - \exp(-k(L+dL)\Omega)}{kdL} = \Omega\exp(-kL\Omega) \quad (1)$$

All symbols are defined in Appendix A. The list of optical parameters appears in Table S1 in the auxiliary material.[1] Note that Ω was multiplied before the exponential term too (Ω exp($-kL\Omega$)). For a canopy with a random leaf spatial distribution, Ω = 1 and equation (1) becomes the conventional gap fraction equation (= exp($-kL$)).

2.1.2.1. Absorbed Photosynthetically Active Radiation by Sunlit and Shade Leaves

[13] We modified the PAR penetration model [*de Pury and Farquhar*, 1997], by incorporating foliar clumping effects and reflected PAR from the soil. We replaced exp ($-kL$) in the work by *de Pury and Farquhar* [1997] with equation (1), and re-derived the set of equations that depend upon this relation. Total absorbed incoming PAR by the canopy (Q_P) is

$$Q_{p\downarrow} = (1-\rho_{cbP})I_{Pb}(0)[1-\exp(-k'_{Pb}L_c\Omega)] + (1-\rho_{cdP})I_{Pd}(0)[1-\exp(-k'_{Pd}L_c\Omega)] \quad (2)$$

where 0 and L_c indicate the leaf area index at the top and the bottom of the canopy, respectively. ρ_{cbP} and ρ_{cdP} are canopy reflectance for beam PAR and diffuse PAR, respectively. I_{Pb} and I_{Pd} are direct beam PAR and diffuse PAR, respectively. k'_{Pb} and k'_{Pd} are extinction coefficient for beam and scattered beam PAR, and for diffuse and scattered diffuse PAR, respectively.

[14] The absorbed incoming beam PAR by sunlit leaves (Q_{PbSun}) is

$$Q_{PbSun\downarrow} = I_{Pb}(0)(1-\sigma_{PAR})[1-\exp(-k_bL_c\Omega)] \quad (3)$$

where σ_{PAR} is leaf scattering coefficient for PAR. k_b is extinction coefficient for black leaves.

[15] The absorbed incoming diffuse PAR by sunlit leaves (Q_{PdSun}) is

$$Q_{PdSun\downarrow} = I_{Pd}(0)(1-\rho_{cdP})[1-\exp(-(k'_{Pd}+k_b)L_c\Omega)]k'_{Pd}/(k'_{Pd}+k_b) \quad (4)$$

The absorbed incoming scattered PAR by sunlit leaves (Q_{PsSun}) is

$$Q_{PsSun\downarrow} = I_{Pb}(0)[(1-\rho_{cbP})(1-\exp(-(k'_{Pb}+k_b)L_c\Omega))k'_{Pb}/(k'_{Pb}+k_b) - (1-\sigma_{PAR})(1-\exp(-2k_bL_c\Omega))/2] \quad (5)$$

[1] Auxiliary materials are available in the HTML. doi:10.1029/2011GB004053.

The total absorbed incoming PAR by sunlit leaves is

$$Q_{PSun\downarrow} = Q_{PbSun\downarrow} + Q_{PdSun\downarrow} + Q_{PsSun\downarrow} \quad (6)$$

The total absorbed incoming PAR by shade leaves is

$$Q_{PSh\downarrow} = Q_{P\downarrow} - Q_{PSun\downarrow} \quad (7)$$

A proportion of the incoming PAR penetrates through the canopy to the soil surface and is reflected up into the canopy, which could be significant in open canopy with bright background. The PAR absorbed by the sunlit leaves as a result of that reflected by the soil is

$$Q_{PSun\uparrow} = \left[(1-\rho_{cbP})I_{Pb}(0) + (1-\rho_{cdP})I_{Pd}(0) - \left(Q_{PSun\downarrow} + Q_{Psh\downarrow}\right)\right] \times \rho_{sP} \times \exp(-k'_{Pd}L_c\Omega) \quad (8)$$

where ρ_{sP} is soil reflectance for PAR.

[16] The PAR absorbed by the shade leaves as a result of that reflected by the soil is

$$Q_{PSh\uparrow} = \left[(1-\rho_{cbP})I_{Pb}(0) + (1-\rho_{cdP})I_{Pd}(0) - \left(Q_{PSun\downarrow} + Q_{Psh\downarrow}\right)\right] \times \rho_{sP} \times [1-\exp(-k'_{Pd}L_c\Omega)] \quad (9)$$

Finally, the total PAR absorbed by the sunlit and shade leaves is

$$Q_{PSun} = Q_{PSun\downarrow} + Q_{PSun\uparrow} \quad (10)$$

$$Q_{PSh} = Q_{PSh\downarrow} + Q_{PSh\uparrow} \quad (11)$$

2.1.2.2. Absorbed Near-Infrared Radiation by Sunlit and Shade Leaves

[17] The absorbed NIR by canopy has the same form as the absorbed PAR in the canopy. However, the canopy radiative transfer of NIR differs from PAR because photons are scattered more in the NIR region within the canopy. *Goudriaan* [1977] showed that the NIR penetration may follow the Beer's law after modifying the extinction coefficient for beam and scattered beam NIR (k'_{Nb}) and for diffuse and scattered diffuse NIR (k'_{Nd}):

$$k'_{Nb} = k_b\sqrt{1-\sigma_{NIR}} \quad (12)$$

$$k'_{Nd} = 0.35\sqrt{1-\sigma_{NIR}} \quad (13)$$

where σ_{NIR} is leaf scattering coefficient for NIR.

[18] The total incoming NIR absorbed by sunlit leaves is

$$\begin{aligned} Q_{NSun\downarrow} &= I_{Nb}(0)(1-\sigma_{NIR})(1-\exp(-k_bL_c\Omega)) \\ &+ I_{Nd}(0)(1-\rho_{cdN})(1-\exp(-(k'_{Nd}+k_b)L_c\Omega))k'_{Nd}/(k'_{Nd}+k_b) \\ &+ I_{Nb}(0)[(1-\rho_{cbN})(1-\exp(-(k'_{Nb}+k_b)L_c\Omega))k'_{Nb}/(k'_{Nb}+k_b) \\ &- (1-\sigma_{NIR})(1-\exp(-2k_bL_c\Omega))/2] \end{aligned} \quad (14)$$

where ρ_{cbN} and ρ_{cdN} are canopy reflectance for beam NIR and diffuse NIR, respectively. I_{Nb} and I_{Nd} are direct beam NIR and diffuse NIR, respectively. k'_{Nb} and k'_{Nd} are extinction coefficient for beam and scattered beam NIR, and for diffuse

and scattered diffuse NIR, respectively. σ_{NIR} is leaf scattering coefficient for NIR.

[19] The total incoming NIR absorbed by shade leaves is

$$Q_{NSh\downarrow} = (1-\rho_{cbN})I_{Nb}(0)(1-\exp(-k'_{Nb}L_c\Omega)) + (1-\rho_{cdN})I_{Nd}(0)(1-\exp(-k'_{Nd}L_c\Omega)) - Q_{NSun\downarrow} \quad (15)$$

The NIR absorbed by sunlit leaves as a result of that reflected by the soil is

$$Q_{NSun\uparrow} = \left[(1-\rho_{cbN})I_{Nb}(0) + (1-\rho_{cdN})I_{Nd}(0) - \left(Q_{NSun\downarrow} + Q_{Nsh\downarrow}\right)\right] \times \rho_{sN} \times \exp(-k'_{Nd}L_c\Omega) \quad (16)$$

where ρ_{sN} is soil reflectance for NIR.

[20] The NIR absorbed by shade leaves as a result of that reflected by the soil is

$$Q_{NSh\uparrow} = \left[(1-\rho_{cbN})I_{Nb}(0) + (1-\rho_{cdN})I_{Nd}(0) - \left(Q_{NSun\downarrow} + Q_{Nsh\downarrow}\right)\right] \times \rho_{sN} \times [1-\exp(-k'_{Nd}L_c\Omega)] \quad (17)$$

Finally, total NIR absorbed by sunlit and shade leaves is

$$Q_{NSun} = Q_{NSun\downarrow} + Q_{NSun\uparrow} \quad (18)$$

$$Q_{NSh} = Q_{NSh\downarrow} + Q_{NSh\uparrow} \quad (19)$$

2.1.2.3. Absorbed Longwave Radiation by Sunlit and Shade Leaves

[21] We calculated longwave radiation absorbed by sunlit (Q_{LSun}) and shade leaves (Q_{LSh}) using the *Wang and Leuning* [1998] model.

$$Q_{LSun} = -k'_L\sigma T_a^4(\varepsilon_l(1-\varepsilon_a)(1-\exp(-(k_b+k'_L)L_c))/(k_b+k'_L) + (1-\varepsilon_s)(\varepsilon_l-\varepsilon_a)(1-\exp(-2k'_LL_c))/(2k'_L) \cdot (1-\exp(-(k_b-k'_L)L_c))/(k_b-k'_L)) - c_pg_r(T_{Sun}-T_a) \quad (20)$$

where k'_L is extinction coefficient for longwave radiation. ε_a, ε_l and ε_s are emissivity for air, leaf and soil, respectively. c_p is specific heat of the air, g_r is radiative conductance. T_{Sun} and T_a are sunlit leaf and air temperature, respectively.

$$Q_{LSh} = -k'_L\sigma T_a^4(\varepsilon_l(1-\varepsilon_a)(1-\exp(-k'_LL_c))/k'_L - (1-\varepsilon_s) \cdot (\varepsilon_l-\varepsilon_a) \times \exp(-k'_LL_c)(1-\exp(-k'_LL_c))/k'_L) - Q_{LSun} - c_pg_r(T_{Sun}-T_a) - c_pg_r(T_{Sh}-T_a) \quad (21)$$

where T_{Sh} is shade leaf temperature.

2.1.2.4. Net Radiation

[22] We calculated net radiation by extending the MODIS derived clear sky net radiation scheme [*Ryu et al.*, 2008a] into the whole sky condition that includes clear and cloudy conditions. The atmospheric radiative transfer model enabled us to calculate the incoming shortwave radiation under the whole sky condition. We briefly present the procedure used in the net radiation calculation here. The outgoing shortwave radiation was calculated as the product of incoming solar radiation and land surface albedo from MODIS (MCD43B3). For the cloudy days, we used the white-sky albedo which represents the albedo for diffuse conditions. For the clear sky days, we calculated actual albedo by using a look-up-table provided by Boston University MODIS BRDF project (http://www-modis.bu.edu/brdf/userguide/tools.html). The look-up-table requires solar zenith angle, aerosol optical thickness, which all derived from the MOD04_L2 (aerosol product). For the incoming longwave radiation, we used the *Prata* [1996] model. Input data include air and dew point temperature at the screen level, which were derived from MOD07_L2 (atmospheric profile product). Under cloudy conditions when the MOD07_L2 does not provide temperature information, we used the NCEP/NCAR reanalysis derived temperature data included in MOD06_L2 only. The fraction of cloud cover per each pixel was extracted from MOD06_L2 (1 km), and the incoming longwave radiation for clear [*Prata*, 1996] and cloudy (σT_a^4) conditions were combined to produce the incoming longwave radiation per each pixel [*Crawford and Duchon*, 1999]. The outgoing longwave radiation was calculated using land surface emissivity and land surface temperature from MOD11_L2 (land surface temperature product). For the cloudy sky areas, we used the land surface temperature from the NCEP/NCAR reanalysis data.

2.1.3. Photosynthesis

[23] We used the biochemical photosynthesis models for C3 [*Collatz et al.*, 1991; *Farquhar et al.*, 1980] and C4 plants [*Collatz et al.*, 1992]. The information on the proportion of C3 and C4 plants per pixel is given in section 2.4.3. The two-leaf canopy photosynthesis was calculated using:

$$A_{c,j} = \min\left\{A_{l,j}, A_{v,j}, A_{s,j}\right\} - R_{c,j} \quad (22)$$

where j = *Sun or Sh* indicate sunlit or shade leaf, respectively.

[24] A_l is the light limited rate of CO_2 assimilation (see symbols in Appendix A):

$$A_{l,j} = J_{\max,j}\frac{p_i-\Gamma_{*,j}}{4\left(p_i+2\Gamma_{*,j}\right)} \text{ for C3 species} \quad (23a)$$

$$A_{l,j} = 0.067 \times Q_{Pj} \text{ for C4 species} \quad (23b)$$

[25] A_v is the rubisco limited rate of CO_2 assimilation:

$$A_{v,j} = V_{\max,j}\left(\frac{p_i-\Gamma_{*,j}}{p_i+K_{c,j}\left(1+O/K_{o,j}\right)}\right) \text{ for C3 species} \quad (24a)$$

$$A_{v,j} = V_{\max,j} \text{ for C4 species} \quad (24b)$$

[26] A_s is the capacity for the export or utilization of the products of photosynthesis for C3 species, and CO_2 limited flux for C4 species:

$$A_{s,j} = 0.5V_{\max,j} \text{ for C3 species} \quad (25a)$$

$$A_{s,j} = 0.7 \times 10^6 \times \frac{p_i}{P} \text{ for C4 species} \quad (25b)$$

We fixed the ratio of leaf internal CO_2 concentration to the ambient CO_2 concentration as 0.7 (C3 species) and 0.4 (C4 species) [*Baldocchi*, 1994; *Jones*, 1992; *Norman*, 1982; *Wong et al.*, 1979].

[27] R_c is the two-leaf canopy respiration.

$$R_{c,j} = V^{25C}_{\max,j} \times 0.015 \times \exp\{E_a\_K_c(T_j - 298)/(298 \times R \times T_j)\} \quad \text{for C3 species} \tag{26a}$$

$$R_{c,j} = V^{25C}_{\max,j} \times 0.025 \times 2^{\{(T_j-298)/10/(1+\exp(1.3\times(T_j-328)))\}} \quad \text{for C4 species} \tag{26b}$$

2.1.4. Maximum Carboxylation Rate (V_{max})

[28] The V_{max} is a key parameter in the Farquhar photosynthesis model [*Farquhar et al.*, 1980; *Houborg et al.*, 2009; *Wang et al.*, 2007]. Previous studies used a constant V_{max} for each PFT over the year [*Baldocchi and Wilson*, 2001; *Chen et al.*, 1999; *Cramer et al.*, 2001]. Here we parameterized V_{max} using albedo-*N* relation or look-up-table that classified V_{max} based on PFT and climatic zones, then we varied V_{max} over the season.

[29] We used the albedo-*N* relation for closed-canopy temperate and boreal forests where the relation was tested [*Hollinger et al.*, 2010; *Ollinger et al.*, 2008]:

$$N(\%) = (\alpha - 0.02)/0.067 \tag{27}$$

where α is shortwave albedo.

[30] The *N*(%) was converted to leaf mass per area, then converted to *N*(area) based on a global data set of leaf traits [*Schulze et al.*, 1994; *Wright et al.*, 2004]:

$$LMA = 10^{2.24} N(\%)^{-0.97} \tag{28}$$

$$N(area) = 10^{-0.52} LMA^{0.38} \tag{29}$$

Finally, the *N*(area) was converted to V_{max}@25C (V^{25C}_{max}) by multiplying by the Nitrogen use efficiency (NUE (Table S2), the ratio of V^{25C}_{max} to *N* (g m^{-2}), μmolCO_2 gN^{-1} s^{-1}) which was estimated using 723 data points [*Kattge et al.*, 2009]. For open canopies, non-woody vegetation, or PFTs located in arid and tropical climatic zones, we used V^{25C}_{max} values based on a literature survey that considered both PFT and climatic zones (see section 2.4.4) (Table S2). We assigned vegetation to 'open canopy' if the gap fraction of the zenith direction at peak *L* is higher than 0.3 (i.e., $\exp(-0.5\ L\Omega) > 0.3$).

[31] We considered the seasonal variation of V^{25C}_{max} [*Kosugi et al.*, 2003; *Limousin et al.*, 2010; *Xu and Baldocchi*, 2003], as it proved critical to calculate canopy fluxes accurately [*Houborg et al.*, 2009; *Muraoka et al.*, 2010; *Reichstein et al.*, 2003]. We assumed that the seasonal pattern of V^{25C}_{max} followed the seasonal pattern of *L* [*Houborg et al.*, 2009]. This pattern has been observed previously in temperate forests [*Hikosaka et al.*, 2007; *Kosugi et al.*, 2003; *Muraoka et al.*, 2010; *Wang et al.*, 2008; *Wilson et al.*, 2001] and Mediterranean forests [*Reichstein et al.*, 2003; *Xu and Baldocchi*, 2003]. For each individual pixel, we selected the date when MODIS LAI showed the peak value. We quantified the V^{25C}_{max} for that date (PeakV^{25C}_{max}), then calculated V^{25C}_{max} over the season:

$$V^{25C}_{\max} = a \times PeakV^{25C}_{\max} + (1-a) \times PeakV^{25C}_{\max} \times \frac{L_c - L_{\min}}{L_{\max} - L_{\min}} \tag{30}$$

where L_{max}, L_{min} and L_c are maximum, minimum and current leaf area index over the year. We determined the threshold, *a*, as 0.3 arbitrarily. We calculated the maximum rate of electron transport (J^{25C}_{max}) using a linear relation with V^{25C}_{max} [*Wullschleger*, 1993]:

$$J^{25C}_{\max} = 29.1 + 1.64 \times V^{25C}_{\max} \tag{31}$$

We upscaled the leaf-level V^{25C}_{max} to the canopy level. The total V^{25}_{max} in the canopy ($V^{25C}_{max,tot}$) is:

$$V^{25C}_{\max,tot} = L_c V^{25C}_{\max} \times [1 - \exp(-k_n)]/(k_n) \tag{32}$$

where k_n is the nitrogen extinction coefficient, and we assumed it is same as the beam and scattered beam PAR extinction coefficient (k'_{Pb}) for optimal carbon gain [*Anten et al.*, 1995; *Hikosaka*, 2003].

[32] The sunlit canopy V^{25C}_{max} is

$$V^{25C}_{\max,sun} = L_c V^{25C}_{\max} \times \frac{1}{k_n + k_b L_c}[1 - \exp(-(k_n + k_b L_c))] \tag{33}$$

The shaded canopy V^{25C}_{max} is

$$V^{25C}_{\max,sh} = V^{25C}_{\max,tot} - V^{25C}_{\max,sun} \tag{34}$$

The J^{25C}_{max} was upscaled to the two-leaf canopy in a same manner as V^{25C}_{max}. Both $V^{25C}_{max,j}$ and $J^{25C}_{max,j}$ for the two leaf canopy (*j* = sun or shade) was converted to the values at the actual air temperature ($V_{max,j}$ and $J_{max,j}$) using a temperature correction function [*Kattge and Knorr*, 2007].

2.1.5. Two-Leaf Canopy Conductance and Temperature

[33] We used Ball-Berry equation to calculate two-leaf canopy conductance [*Ball*, 1988]:

$$G_{c,j} = m\frac{A_{c,j} RH}{C_a} + b \tag{35}$$

We fixed the Ball-Berry slope (*m*) as 10 for C3 species [*Collatz et al.*, 1991; *Harley and Baldocchi*, 1995; *Harley et al.*, 1992; *Xu and Baldocchi*, 2003], and 4 for C4 species [*Collatz et al.*, 1992; *Hanan et al.*, 2005].

[34] The enzymatic activity in the photosynthesis models changes with leaf temperature, thus getting the correct leaf temperature is important. We used an analytic solution based on leaf energy balance to calculate two-leaf temperatures [*Paw U and Gao*, 1988]. However, as the solution requires $G_{c,j}$ as an input variable, which needs T_j for photosynthesis calculation, we iteratively calculated $A_{c,j}$, $G_{c,j}$, and T_j until convergence. The Ball-Berry equation enabled an explicit coupling of photosynthesis and evapotranspiration, although the two '*m*' values could be refined [*Law et al.*, 2001].

2.1.6. Evapotranspiration

[35] We used a quadratic form of the Penman-Monteith equation to calculate the two-leaf canopy latent heat flux (λE_j, j = sun or shade) [*Monteith*, 1965; *Paw U and Gao*, 1988]. This approach uses the second order Taylor expansion to estimate saturated vapor pressure at the leaf surface using air temperature; on the other hand, the conventional Penman Monteith equation uses the first order Taylor expansion (i.e., linearization). When the temperature difference between the air and leaf is large (e.g., >5°C), the first order approximation can underestimate λE by 10–20% [*Paw and Gao*, 1988]. Because BESS is designed for global applications, we adopted the quadratic form of the Penman-Monteith equation, which requires exactly the same input variables as the conventional Penman-Monteith equation:

$$a\lambda E_j^2 + b\lambda E_j + c = 0, \tag{36a}$$

where

$$a = \frac{{r_a}^2}{2\left[\rho_a C_p \gamma\left(r_a + r_{c,j}\right)\right]} \frac{d^2 e_s(T_a)}{d{T_a}^2} \tag{36b}$$

$$b = -1 - r_a \frac{de_s(T_a)}{dT_a} \frac{1}{\gamma\left(r_a + r_{c,j}\right)} - \frac{R_{n,j} {r_a}^2}{\rho_a C_p \gamma\left(r_a + r_{c,j}\right)} \frac{d^2 e_s(T_a)}{d{T_a}^2} \tag{36c}$$

$$c = \frac{\rho_a C_p D}{\gamma\left(r_a + r_{c,j}\right)} + \frac{r_a R_{n,j}}{\gamma\left(r_a + r_{c,j}\right)} \frac{de_s(T_a)}{dT_a} + \frac{1}{2} \frac{\left(r_a \times R_{n,j}\right)^2}{\rho_a C_p \gamma\left(r_a + r_{c,j}\right)} \cdot \frac{d^2 e_s(T_a)}{d{T_a}^2} \tag{36d}$$

where r_a and $r_{c,j}$ are aerodynamic and canopy (j represents sunlit or shade leaf) resistance, respectively. ρ_a is air density. γ is psychrometric constant. $e_s(T)$ is saturated vapor pressure at temperature, T [*Henderson-Sellers*, 1984]. $R_{n,\ j}$ is net radiation (j represents sunlit or shade leaf).

[36] The two-leaf λE_j shares all input variables except for $r_{c,j}$ and $R_{n,j}$.

[37] We calculated soil evaporation (λE_{soil}) using a simple equilibrium evaporation model constrained by a soil water stress function. It was reported that soil litter layer substantially controls on the soil evaporation [*Baldocchi et al.*, 2000; *Lee and Mahrt*, 2004; *Wilson et al.*, 2000]; however, due to the lack of soil litter layer information at global scale, we adopted a simple approach:

$$\lambda E_{soil} = \frac{s}{s+\gamma}\left(R_{n,soil} - G_{soil}\right) \times RH^{D/1000} \tag{37}$$

The soil water stress function ($RH^{D/1000}$) was proposed in *Fisher et al.* [2008]. The $R_{n,soil}$ is net radiation at the soil surface:

$$R_{n,soil} = R_n - \left(R_{n,Sun} + R_{n,Sh}\right) \tag{38}$$

G_{soil} is the soil heat flux:

$$G_{soil} = 0.35 \times R_{n,soil} \tag{39}$$

The constant of 0.35 was the mean between its likely limits of 0.2 and 0.5 [*Choudhury et al.*, 1987].

2.2. MODIS-Azure Cloud Computing Service

[38] BESS requires downloading, standardizing and processing approximately 15 terabytes of MODIS data. We built the MODIS-Azure service on the Microsoft Azure cloud computing platform to operate BESS system [*Agarwal et al.*, 2011; *Li et al.*, 2010]. The basic idea is "download MODIS data to the Cloud, process/analyze data in the Cloud, and download results from the Cloud to my PC" (Figure 2). The MODIS-Azure web portal allows 1) submitting job requests and 2) monitoring the processing job status in real-time. One can request the number of virtual machines (1–250 virtual machines currently) depending on the estimated computing needs, which offer highly scalable performance. As shown in Figure 2, after a scientist submits a computation request to the MODIS-Azure system through the Web portal, the request is sent to the Azure system for processing. First, all the required source product data are automatically downloaded from the external MODIS data FTP sites to the Azure storage; the geographic metadata information for all data files are also maintained in Azure storage. Second, all Level 2 MODIS products (swath type) are reprojected into sinusoidal projection as used in Levels 3, 4, and 5 in MODIS Land products. These steps are performed as necessary to satisfy the needs of the science computation and the results are cached in Azure storage. Third, an executable file encoded with the scientists' computation algorithm is executed at individual virtual machines in parallel to produce the final results. Finally, a download link to the final result data produced by the computation is sent to the scientist in a notification email. Detailed description on the MODIS-Azure system is given by *Li et al.* [2010].

2.3. Processing MODIS Data

2.3.1. MODIS Atmospheric Products

[39] We used the MODIS-Azure service to grid Level 2 (swaths) MODIS atmospheric products (collection 5). We followed the MODIS Land tile conventions (sinusoidal tiles, each tile is ~1200 km by ~1200 km) [*Wolfe et al.*, 1998] to standardize the Level 2 MODIS atmospheric products. This step enabled us to co-locate MODIS Land and Atmospheric products. The Level 2 products were gridded for each sinusoidal tile per day using either MOD (Terra) or MYD (Aqua). Primarily, we used MOD (Terra), but when it was not available due to satellite outage, we used MYD (Aqua). The gridded Level 2 MODIS atmospheric products include MO(Y)D04_L2 (aerosol product), MO(Y)D05_L2 (water vapor product), MO(Y)D06_L2 (cloud product), MO(Y)D07_L2 (atmospheric profile product). We determined the sinusoidal tile location first, then the MODIS-Azure system searched all granules that cover the requested tile area using a spatial prescreening technique [*Hua et al.*, 2007] and downloaded the granules from the NASA FTP server (ftp://ladsweb.nascom.nasa.gov/allData/5/). We used an inverse gridding approach [*Konecny*, 1979; *Wolfe et al.*, 1998] to make the sinusoidal tiles of Level 2 MODIS atmospheric products. The spatial resolution of Level 2 MODIS atmospheric products ranges between 1 km (a portion of the cloud product) and 10 km (aerosol product) (Table 1). We gridded

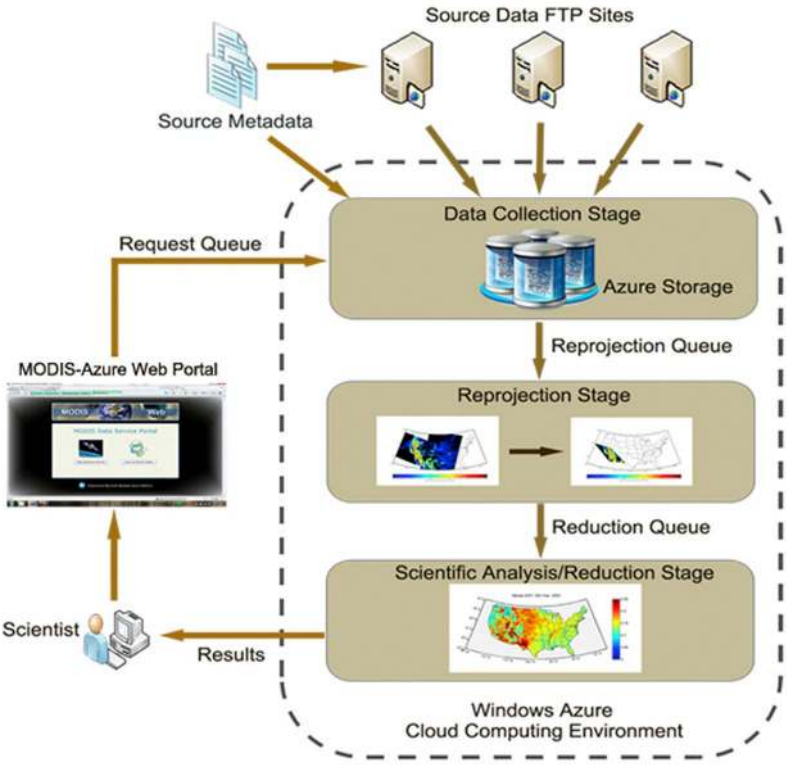

Figure 2. Overview of the MODISAzure system [*Li et al.*, 2010].

the Level 2 MODIS data with a 1 km resolution for the sinusoidal tiles that include the U.S. and the flux towers that were used in this study, and with a 5 km resolution for the other areas to reduce the data size. The air and dew point temperature were retrieved from MO(Y)D07 only for clear sky days [*Houborg et al.*, 2007; *Ryu et al.*, 2008a]. Under cloudy sky days, we used the NCEP/NCAR reanalysis data (see section 2.4.1) to fill the data gaps. The data gaps in aerosol optical depth (MO(Y)D04) were filled using monthly mean aerosol depth.

2.3.2. MODIS Land Products

[40] We used four gridded MODIS Land products (sinusoidal projection) and one swath Land product (MO(Y)D11_L2) (collection 5) (Table 1). The MO(Y)D11_L2 was gridded as done for the L2 MODIS atmospheric products (see section 2.3.1). For the MODIS LAI product (MCD15A2), we only used the data classified as "Main (RT) method used, best result possible (no saturation)" or "Main (RT) method used with saturation. Good, very usable" in the quality flags. For the MODIS albedo product (MCD43B3), we selected the data classified as "best quality, 75% or more with best full inversions" or "good quality, 75% or more with full inversions" in the data quality flag (MCD43B2). The data gaps in the MCD15A2 and MCD43B2 were filled using the following procedures: 1) if at least three years of data exist with acceptable quality among the five years (2001–2005) for the same date, we used the multiyear mean value to fill the data gap for the specific date; this procedure was suggested in the previous studies [*Fang et al.*, 2008, 2007], 2) if unfilled, we applied the information from moving windows with 2, 5, 10 km size at the same tile and used their mean value to fill the data gap, 3) if unfilled, we calculated the mean values for each plant functional type, defined in MODIS land cover product (MCD12Q1), at the same tile, and filled the data gaps using the mean values. For the MODIS albedo product, we separated the data gap filling procedures for snow and snow-free areas [*Fang et al.*, 2007]. The MODIS LAI product in rainfall tropical forests was seriously contaminated by clouds [*Zhao et al.*, 2005], thus we selected the maximum leaf area index in a 8-week interval and kept the value over the 8-weeks. The data gaps in MO(Y)D11_L2 under cloudy condition or satellite outages were filled using the NCEP/NCAR reanalysis skin surface temperature data (see section 2.4.1).

2.4. Ancillary Data

2.4.1. NCEP/NCAR Reanalysis 1

[41] For variables not available from the MODIS system, we retrieved information from the NCEP/NCAR Reanalysis

Table 1. The List of MODIS Data Used in This Study[a]

Product	Name	Spatial Resolution	Temporal Scale
MO(Y)D04_L2	aerosol	10 km	5 min
MO(Y)D05_L2	water vapor	5 km	5 min
MO(Y)D06_L2	cloud	1 km or 5 km	5 min
MO(Y)D07_L2	atmospheric profile	5 km	5 min
MO(Y)D11_L2	land surface temperature	1 km	5 min
MCD12Q1	land cover	0.5 km	yearly
MCD15A2	leaf area index	1 km	8 day
MCD43B2	BRDF-albedo quality	1 km	16 day
MCD43B3	albedo	1 km	16 day

[a]All Land products are version 5. MOD, Terra; MYD, Aqua; MCD, Terra+Aqua.

1 data (Surface Flux) [*Kalnay et al.*, 1996]. The NCEP data set includes information on air temperature, dew point temperature, land surface temperature, and wind speed. The temperature variables (i.e., air, dew point and land surface) were used to fill the data gaps in MODIS which mostly appeared in the cloudy days. The wind speed data were used to calculate aerodynamic conductance. The spatial coverage of NCEP data includes 88.542N-88.542S, 0E-358.125E with a T62 Gaussian grid (192 × 94 points). Its temporal resolution is 6-hourly. We linearly interpolated the 6-hourly data to match with the time stamp of the MODIS data. To remove the abrupt change on the boarders between the coarse pixels, we applied a 3 by 3 moving window average. The NCEP data was resampled using the nearest neighborhood method with the sinusoidal projection at a 1 km resolution.

2.4.2. Global Foliar Clumping Index Map

[42] To consider non-randomness of leaf distribution in space, we used the global foliar clumping index map developed using the multiangle remote sensing data, POLDER 3 [*Chen et al.*, 2005; *Pisek et al.*, 2010]. It offers the clumping index in the growing season at a 6 km resolution. It was resampled using the nearest neighborhood method with the sinusoidal projection at a 1 km resolution.

2.4.3. Global C3 and C4 Distribution Map

[43] To incorporate different ecophysiological processes between C3 and C4 species, we used the global C3 and C4 distribution map [*Still et al.*, 2003]. It offers the proportion of C4 species per pixel at a 1 degree resolution. To remove the abrupt change on the boarders between the coarse pixels, we applied a 3 by 3 moving window average. We resampled using the nearest neighborhood method with the sinusoidal projection at a 1 km resolution. The two-leaf model was performed for the C3 and C4 species separately in a pixel, and the sum of relative proportion of C3 and C4 for the pixel determined the GPP and ET at the pixel.

2.4.4. Köppen-Geiger Global Climate Classification Map

[44] To incorporate the information of climate zone into the look up table of the V_{max}^{25C} where the N-albedo relation was not applied, we used the Köppen-Geiger global climate classification map which represented the average condition between 1951 and 2000 [*Kottek et al.*, 2006]. We used the classification on the main climates that include equatorial, arid, warm temperate, snow, and polar. It provides 0.5 degree resolution. We resampled using the nearest neighborhood method with the sinusoidal projection at a 1 km resolution.

2.5. Temporal Upscaling From Snap-Shots to 8-Day Mean Daily Sums

[45] BESS system quantifies instantaneous GPP and ET first as the radiation components, the main driver of GPP and ET, are derived from the MODIS snap-shots. We upscaled instantaneous GPP and ET estimates to an 8-day mean daily based on a recent study [*Ryu et al.*, 2012]. The potential solar radiation (R_{gPOT}) can be easily calculated with only a few basic pieces of information on the Sun-Earth geometry [*Liu and Jordan*, 1960]:

$$R_{gPOT} = S_{sc} \times [1 + 0.033\cos(2\pi t_d/365)]\cos\beta \quad (40)$$

where S_{sc} is the solar constant (1368 W m^{-2}), t_d is the day of year, and β is solar zenith angle that is calculated following *Michalsky* [1988]. The upscaling factor is defined as:

$$SF_d(t) = \frac{1800s \times \lambda E(t)}{\int_d \lambda E(t)dt} \approx \frac{1800s \times R_{gPOT}(t)}{\int_d R_{gPOT}(t)dt} \quad (41)$$

where SF_d(t) is the upscaling factor for a particular day ($_d$) of the year and function of the time t of the instantaneous λE. The 1800s is the number of seconds in 30 min. Then the 8-day mean daily sum λE is:

$$\lambda E_{8day} = \frac{1}{8}\sum_{d=1}^{8} \frac{1800s \times \lambda E(t_d)}{SF_d(t_d)} \quad (42)$$

where the time of the snapshot, t_d, may change between one day and another accordingly to the satellite passages.

[46] This temporal upscaling scheme was tested against data from 33 flux towers across seven plant functional types from boreal to tropical climatic zones. The results showed that the upscaled and measured 8-day mean daily sum ET showed a strong linear relation (r^2 = 0.92) and small bias (−2.7%) [*Ryu et al.*, 2012]. Furthermore, it was found that the temporal upscaling scheme can be used to upscale instantaneous estimates of GPP and solar irradiance to 8-day mean daily sum estimates as accurately as ET.

2.6. Flux Tower Data and Evaluation of BESS

[47] To test BESS, we used data from 33 flux towers that cover seven plant functional types (PFT) across arctic to tropical climatic zones to test simulations of water and carbon fluxes from BESS (Table 2, the citation for each site is shown in Table S3). The data were extracted from LaThuile 2007 FLUXNET data set v.2 (www.fluxdata.org). We selected at least three sites for each PFT with data gaps less than 30 days per year, and selected one year of measurements per site that was represented by the least of data gaps over the available years. Data gaps were filled using the marginal distribution sampling method in a harmonized and standardized way for the LaThuile 2007 FLUXNET data set [*Reichstein et al.*, 2005].

2.7. Sensitivity Analysis of Evapotranspiration

[48] A non-dimensional relative sensitivity of ET was quantified [*Beven*, 1979; *McCuen*, 1974]:

$$S_i = \frac{\partial ET}{\partial V}\frac{V}{ET} \quad (43)$$

where S_i is the relative sensitivity ranged between −1 (negatively highly sensitive) to 1 (positively highly sensitive), ET is the conventional Penman-Monteith equation [*Monteith*, 1965] to keep simplicity in the differentials, V is the input variable in the Penman Monteith equation such as available energy and canopy conductance. The sensitivity of ET to V is very low as the Si approaches to the zero.

3. Results

3.1. Evaluation of BESS Against Flux Tower Data

[49] BESS derived solar irradiance ($R_{s,i}$), GPP and ET at 1 km resolution were evaluated against the flux tower data

Table 2. Flux Tower Site Information[a]

PFT	Site ID	Site Name	Latitude	Longitude	Year	Climate
CRO	U.S.-Bo1	Bondville	40.0	−88.3	1998	Temperate (Dfa)
	DE-Geb	Gebesee	51.1	10.9	2004	Temperate (Cfb)
	U.S.-Ne1	Mead–irrigated continuous maize site	41.2	−96.5	2004	Temperate (Dfa)
DBF	CA-Oas	Sask.–SSA Old Aspen	53.6	−106.2	2004	Boreal (Dfc)
	DE-Hai	Hainich	51.1	10.5	2004	Temperate (Cfb)
	U.S.-MOz	Missouri Ozark Site	38.7	−92.2	2005	subtropical, Mediterranean (Cfa)
	U.S.-Bar	Bartlett Experimental Forest	44.1	−71.3	2005	temperate (Dfb)
	JP-Tak	Takayama	36.1	137.4	2003	temperate-continental (Dfb)
	U.S.-MMS	Morgan Monroe State Forest	39.3	−86.4	2003	subtropical, Mediterranean (Cfa)
	U.S.-UMB	Univ. of Mich. Biological Station	45.6	−84.7	2003	temperate-continental (Dfb)
EBF	BR-Ji2	Rond.–Rebio Jaru Ji Parana–Tower A	−10.1	−61.9	2001	tropical (Aw)
	BR-Sa1	Santarem-Km67-Primary Forest	−2.9	−55.0	2003	tropical (Am)
	BR-Sa3	Santarem-Km83-Logged Forest	−3.0	−54.5	2003	tropical (Am)
	VU-Coc	CocoFlux	−15.4	167.2	2003	tropical (Af)
	AU-Tum	Tumbarumba	−35.7	148.2	2003	temperate (Cfb)
	ID-Pag	Palangkaraya	2.3	114.0	2002	tropical (Af)
ENF	FI-Hyy	Hyytiala	61.8	24.3	2006	boreal (Dfc)
	CA-Obs	Sask.–SSA Old Black Spruce	54.0	−105.1	2003	boreal (Dfc)
	CA-Ojp	Sask.–SSA Old Jack Pine	53.9	−104.7	2003	boreal (Dfc)
	RU-Fyo	Fedorovskoje-drained spruce stand	56.5	32.9	2003	temperate-continental (Dfb)
	U.S.-Wrc	Wind River Crane Site	45.9	−122.0	2004	subtropical, Mediterranean (Csb)
	U.S.-Me2	Metolius-intermediate aged ponderosa pine	44.5	−121.6	2004	subtropical, Mediterranean (Csb)
	U.S.-Me3	Metolius-second young aged pine	44.3	−121.6	2004	subtropical, Mediterranean (Csb)
	DE-Tha	Tharandt- Anchor Station	51.0	13.6	2004	temperate (Cfb)
GRA	CN-HaM	Haibei Alpine Tibet site	37.4	101.2	2003	Arctic (ET)
	CA-Let	Lethbridge	49.7	−112.9	2005	temperate (Dfb)
	DE-Meh	Mehrstedt 1	51.3	10.7	2005	temperate (Cfb)
MF	JP-Tom	Tomakomai National Forest	42.7	141.5	2003	temperate-continental (Dfb)
	CA-Gro	Groundhog River-Mat. Boreal Mixed Wood	48.2	−82.2	2005	boreal (Dfb)
	CA-WP1	Western Peatland	55.0	−112.5	2005	boreal (Dfc)
WSA	U.S.-SRM	Santa Rita Mesquite	31.8	−110.9	2005	dry (Bsk)
	AU-How	Howard Springs	−12.5	131.2	2003	tropical (Aw)
	U.S.-Ton	Tonzi ranch	38.4	−121.0	2005	subtropical, Mediterranean (Csa)

[a]Abbreviations in the plant functional types (PFT) include: CRO: crop, DBF: deciduous broadleaved forest, EBF: evergreen broadleaved forest, ENF: evergreen needle leaved forest. GRA: grassland, MF: mixed forest, WSA: woody savanna. The abbreviations in the climate (in the parenthesis) followed the Köppen-Geiger global climate classification (see the Figure 7 for the definition of the abbreviations).

at the scale of daily sum averaged over an 8-day interval (Figures 3–5). We selected the pixel that included a flux tower, then compared the BESS-derived estimates with the flux tower measurements. There was a strong linear relation between BESS $R_{s,i}$ and flux tower $R_{s,i}$ ($r^2 > 0.8$) except for the tropical forests (see Table 2 for the list of tropical forests) where the seasonal variation of $R_{s,i}$ was not pronounced (e.g., BR-Ji2 and BR-Sa3, coefficient of

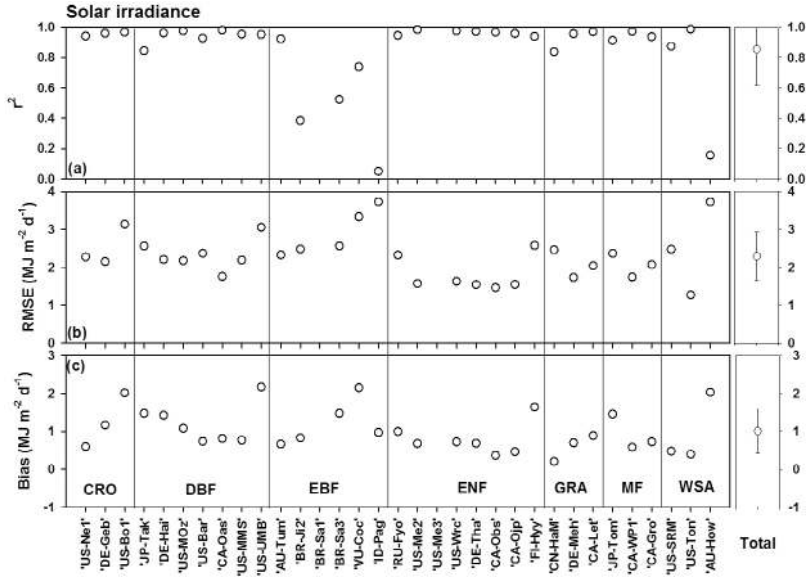

Figure 3. Comparison of 8-day mean daily sum solar irradiance between the 33 flux towers and the BESS.

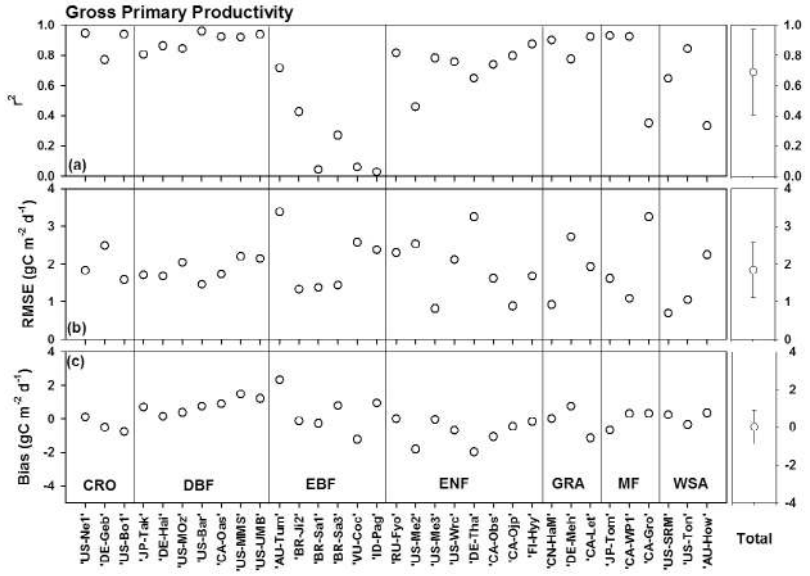

Figure 4. Comparison of 8-day mean daily sum gross primary productivity between the 33 flux towers and the BESS.

variance <15%) or seasonal fires were intense (e.g., ID-Pag and AU-How) (Figure 3). The RMSE varied from 1.2 MJ m^{-2} d^{-1} (U.S.-Ton) to 3.8 MJ m^{-2} d^{-1} (AU-How) with the mean of 2.3 MJ m^{-2} d^{-1}. The bias ranged from 0.2 MJ m^{-2} d^{-1} (CN-HaM) to 2.2 MJ m^{-2} d^{-1} (U.S.-Bo1) with the mean of 1 MJ m^{-2} d^{-1}.

[50] For the GPP, BESS showed low r^2 (<0.4) for the tropical forests where seasonal pattern of GPP was not pronounced (e.g., BR-Sa1, BR-Sa3, ID-Pag, VU-Coc; the coefficient of variance was <20%) (Figure 4). The average of r^2 over the all sites was 0.69. The RMSE and bias varied from 0.7 (U.S.-SRM) to 3.4 (AU-Tum) gC m^{-2} day^{-1}, and −1.8 (U.S.-Me2) to 2.3 (AU-Tum) gC m^{-2} day^{-1}, respectively. The average of RMSE and bias over the all sites were 1.8 and 0.02 gC m^{-2} day^{-1}, respectively. BESS underestimated GPP in all evergreen needleleaf forest sites except for the RU-Fyo site; the bias ranged from 0 (RU-Fyo) to −1.96 (U.S.-Me2) gC m^{-2} day^{-1}. BESS overestimated GPP of all deciduous broadleaved forest sites; the bias ranged from 0.1 (DE-Hai) to 1.5 (U.S.-MMS) gC m^{-2} day^{-1}.

[51] BESS-derived λE showed linear relations with the observed λE from the flux towers ($r^2 > 0.7$) except for the tropical forests (e.g., BR-Sa1, BR-Sa3, ID-Pag, VU-Coc,

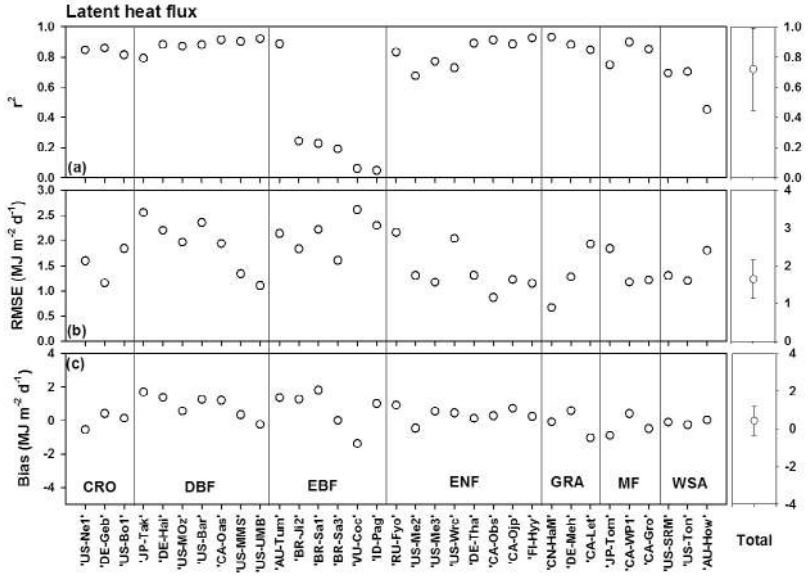

Figure 5. Comparison of 8-day mean daily sum latent heat flux between the 33 flux towers and the BESS.

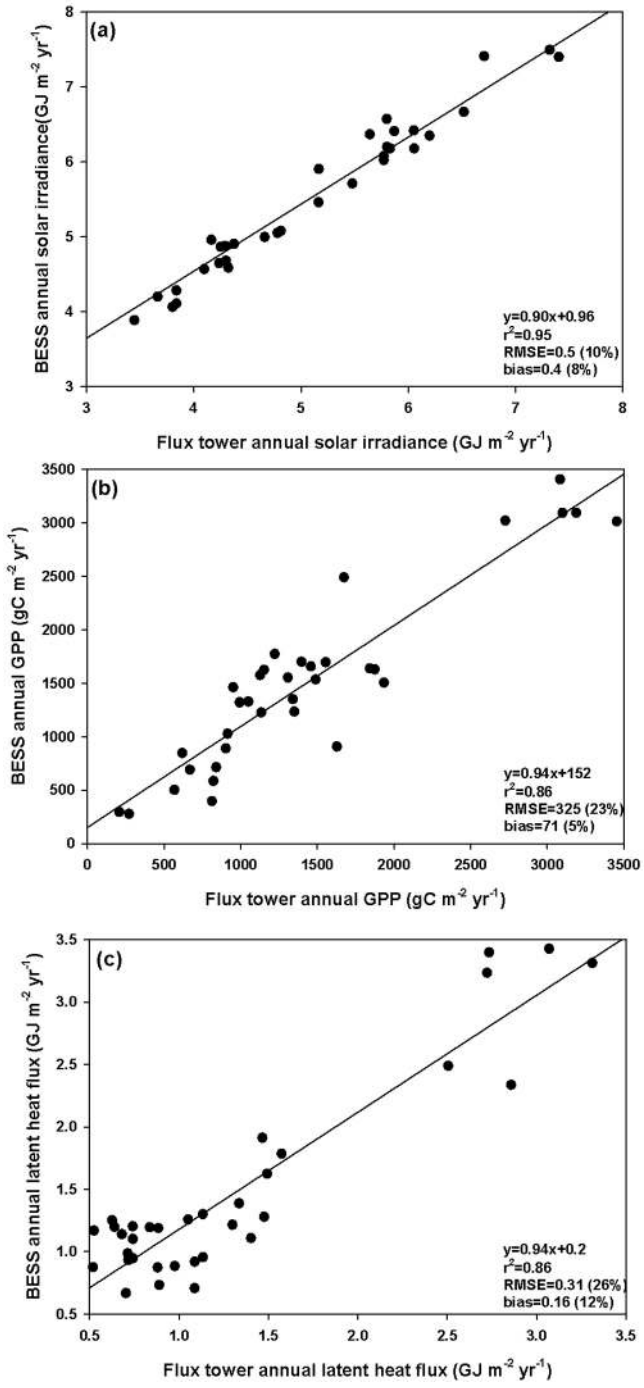

Figure 6. Comparison of (a) annual solar irradiance, (b) gross primary productivity, and (c) latent heat flux between the flux towers and the BESS.

BR-Ji2; coefficient of variance was <25%) (Figure 5). The RMSE and bias varied from 0.7 (CN-HaM) to 2.6 (VU-Coc) MJ m^{-2} d^{-1} and −1.4 (VU-Coc) to 1.8 (BR-Sa1) MJ m^{-2} d^{-1}, respectively. The average of RMSE and bias over the all sites were 1.6 and 0.3 MJ m^{-2} d^{-1}, respectively.

[52] We evaluated the BESS-derived annual sum of $R_{s,i}$, GPP, and λE against the flux tower data (Figure 6). BESS showed strong linear relations with the flux tower data for annual $R_{s,i}$, GPP and λE (r^2 = 0.95, 86, and 86, respectively). All three variables showed positive biases, with overestimates from BESS. Both relative RMSE and bias were higher for λE than GPP.

3.2. Evaluation of BESS Against Data-Driven Products and Basin Water Balance Data

[53] We compared BESS-derived GPP and ET against the empirical flux-tower-data-driven GPP [*Beer et al.*, 2010] and ET [*Jung et al.*, 2010] products for each bioclimatic zone defined from the Köppen-Geiger global climate classification map. The flux-tower-data driven products were developed by formulating statistical models based on the available FLUXNET data, thus they offer "data-driven" but totally empirical estimates [*Jung et al.*, 2009]. We found that BESS-derived GPP showed an excellent agreement with the GPP estimates of *Beer et al.* [2010] with an r^2 of 0.98, 12% of relative RMSE and 0% of relative bias (Figure 7). BESS-derived ET also showed a very good agreement with the ET estimates of *Jung et al.* [2010] with an r^2 of 0.92, 23% of relative RMSE and 0% of relative bias (Figure 8).

[54] We compared the BESS-derived ET against the basin-scale ET derived using a water balance approach (rainfall minus runoff) as reported by *Jung et al.* [2010]. They calculated the annual mean ET for 112 basins (on average, 15 years) using the discharge data from the Global Runoff Data Centre and the rainfall data from the six different rainfall products (see details in auxiliary material) [*Jung et al.*, 2010]. We used BESS-derived mean annual ET over three years (2001–2003) to compare with the water balance derived ET. BESS derived basin ET showed r^2 of 0.78, RMSE of 168 mm yr^{-1}, and bias of 1.9 mm against the water balance derived ET (Figure 8c). For comparison, the data-driven mean annual ET that covered the same period with water-balance ET showed r^2 of 0.92, RMSE of 149 mm yr^{-1}, and bias of 17 mm yr^{-1} of bias against the water balance derived ET [*Jung et al.*, 2010].

3.3. Sensitivity Analysis on BESS-Derived GPP and ET

[55] We performed a simple sensitivity analysis for BESS-derived GPP and ET over the global land in July, 2003 (Figure 9). We selected five variables that included solar irradiance ($R_{s,i}$), leaf area index (L_c), V_{max}^{25C}, vapor pressure deficit (D), and wind speed. We changed the values of each variable by ±30% while keeping the other four variables, and compared the BESS outputs. The consistent relative change for each variable offered all outputs comparable and we assumed the natural variability is well within the range of ±30% of the variables. BESS-derived GPP was most sensitive to the L_c, and next V_{max}^{25}. A 30% change in L_c was associated with a ∼25% change in GPP. A 30% change in V_{max}^{25} was associated with a ∼15% change in GPP. ET was most sensitive to $R_{s,i}$, and next L_c. The 30% change in $R_{s,i}$ was associated with a ∼20% change in ET. For both GPP and ET, BESS was less sensitive to D and wind speed.

[56] The sensitivity of ET to available energy and canopy conductance was investigated (see 2.7) in July 2003 (Figure 10). The ET was highly sensitive to the available energy in the rainfall forests in Amazon, Congo, and Indonesia. The ET was highly sensitive to the canopy conductance in dry region such as mid-west U.S., Spain, Australia and Central Asia.

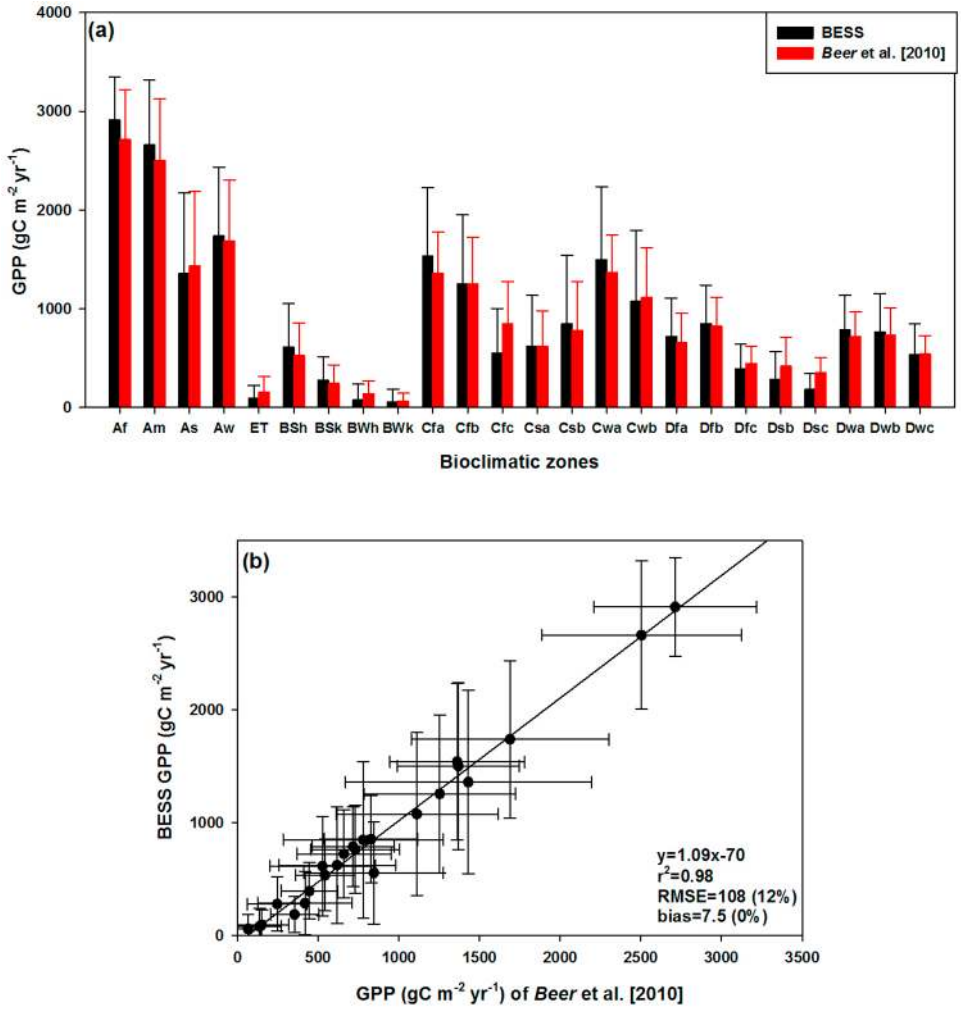

Figure 7. Comparison of gross primary productivity between *Beer et al.* [2010] and the BESS across bioclimatic zones classified by the Köppen-Geiger global climate classification map (see section 2.4.4). The abbreviations for the bioclimatic zones are as follows: Af, equatorial, fully humid; Am, equatorial, monsoonal; As, equatorial, summer dry; Aw, equatorial, winter dry; BWk, cold arid desert; BWh, hot arid desert; BSk, cold arid steppe; BSh, hot arid steppe; Cfa, humid, warm temperate, hot summer; Cfb, humid, warm temperate, warm summer; Cfc, humid, warm temperate, cool summer; Csa, summer dry, warm temperate, warm summer; Csb, summer dry, warm temperate, warm summer; Cwa, winter dry, warm temperate, hot summer; Cwb, winter dry, warm temperate, warm summer; Dfa, snow, humid, hot summer; Dfb, snow, humid, warm summer; Dfc, snow, humid, cool summer; Dsb, snow, summer dry, warm summer; Dsc, snow, summer dry, cool summer; Dwa, snow, winter dry, hot summer; Dwb, snow, winter dry, warm summer; Dwc, snow, winter dry, cool summer; ET, polar tundra.

3.4. Global and Yearly Estimates of Terrestrial GPP and ET

[57] We quantified the mean annual land GPP over the three years (2001–2003) as 118 ± 26 PgC yr^{-1} (or 938 ± 206 gC m^{-2} yr^{-1}) (Figure 11a). To estimate the error bounds, we calculated the mean RMSE between flux tower and BESS for each PFT, assigned the RMSE to the global land which was classified with the same PFT, then quantified the RMSE at global scale. The global annual GPP varied 115, 117, 122 PgC yr^{-1} across the three years. The annual mean global land ET over the same period was 500 ± 104 mm yr^{-1} (equivalent to 63,000 ± 13,100 km^3 yr^{-1}) (Figure 11b). The uncertainty was estimated as done in GPP. The global land ET varied 498, 498, 504 mm yr^{-1} for the three years. For the unit conversion in GPP (PgC yr^{-1} to gC m^{-2} yr^{-1}) and ET (mm yr^{-1} to km^3 yr^{-1}), we used the global land area as 1.26×10^8 km^2 determined from MODIS land cover product. We excluded urban, Greenland, Arctic and Antarctic regions in the land area estimation.

4. Discussion

4.1. Efficacy of BESS

[58] The mechanistic, coupled biophysical model produced reliable estimates of GPP and ET against flux tower data (Figures 4–6), data-driven products (Figures 7 and 8),

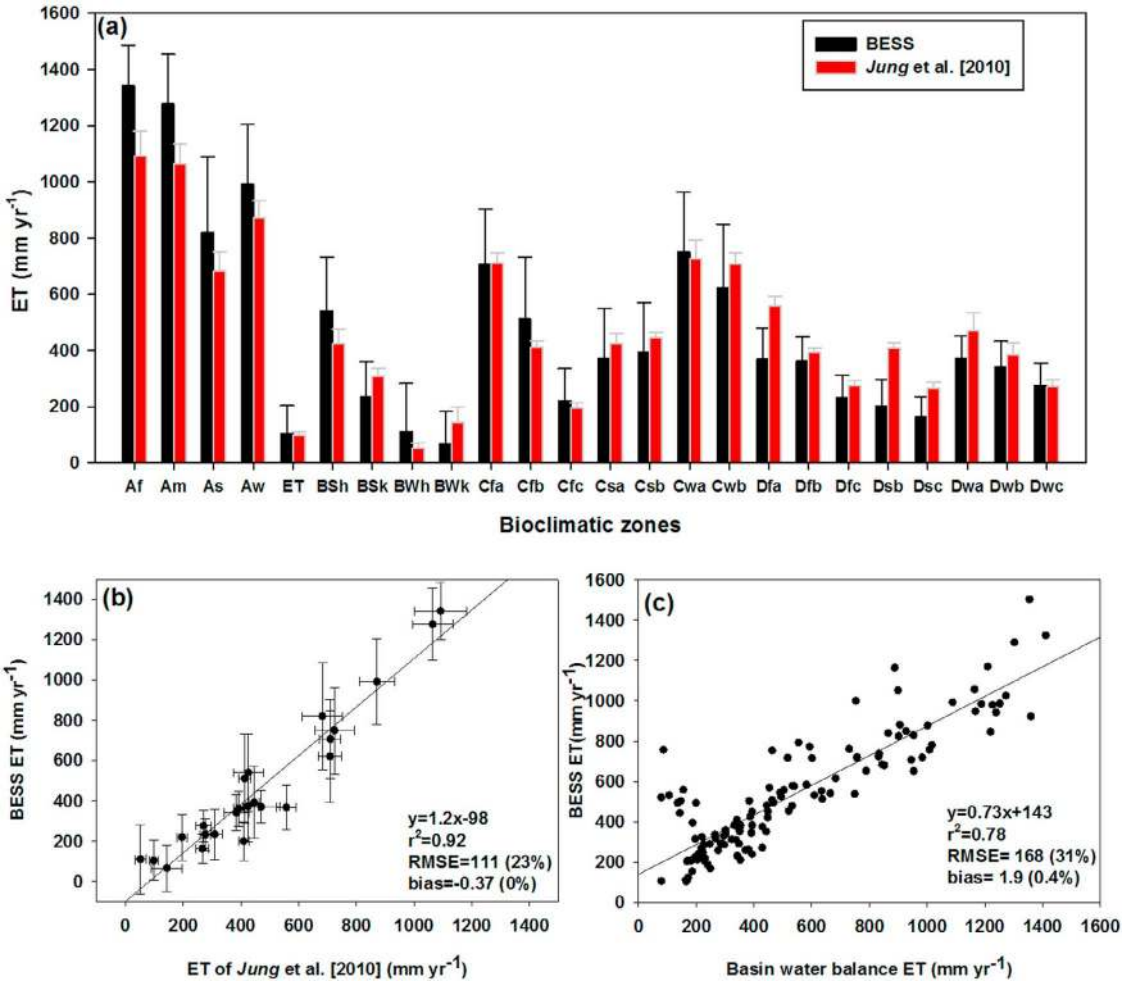

Figure 8. (a and b) Comparison of evapotranspiration between *Jung et al.* [2010] and the BESS across bioclimatic zones classified by the Köppen-Geiger global climate classification map (see section 2.4.4). (c) Comparison of evapotranspiration between the water-balance derived evapotranspiration from global 112 basins (see section 3.2) and the BESS. The abbreviations for the bioclimatic zones are same as in Figure 6.

and basin water balance derived ET (Figure 8c). The formulation of BESS model was entirely independent from flux tower data, which contrast with previous empirical studies that used flux tower data to calibrate key parameters [*Yuan et al.*, 2010; *Zhang et al.*, 2010] or to apply machine-learning technique [*Beer et al.*, 2010; *Jung et al.*, 2010; *Xiao et al.*, 2010]. The success of BESS demonstrates that the advancements in remote sensing, micrometeorology, and ecophysiology enable us to develop a globally applicable model based on first principles, which was discouraged a generation ago due to the concerns about garbage-in and garbage-out [*de Wit*, 1970].

[59] We note that BESS did not explicitly include a soil moisture effect, which is a major factor that limits GPP and ET in water-limited ecosystems [*Ciais et al.*, 2005; *Rambal et al.*, 2003; *Ryu et al.*, 2008b; *Scott et al.*, 2010; *Xu and Baldocchi*, 2004], and evaporation from intercepted rainfall in the canopy, which could be ~20% of rainfall in forests [*Miralles et al.*, 2010]. Why did BESS perform well in spite of the lack in the two terms? BESS assumed that the soil moisture stress is reflected in the seasonal pattern of leaf area index, which in turn influences the seasonal pattern of V_{max}^{25} (see section 2.1.4). We found that this assumption enabled us to capture the seasonal water-limiting effects in most seasonally dry ecosystems such as U.S.-Ton, U.S.-SRM, and AU-How sites. BESS-derived GPP and ET in dry regions were comparable with the data-driven products (Figures 7b and 8b). However, this assumption did not work where MODIS incorrectly quantified leaf area index in semi-arid pine forests that have low seasonality of leaf area index with low annual rainfall and cold winter temperatures (e.g., U.S.-Me2, 535 mm mean annual precipitation [*Thomas et al.*, 2009]; see section 4.2).The evaporation from intercepted rainfall was not explicitly considered in BESS. However, in the wet canopy where intercepted rainfall is dominant, canopy conductance tends to be high (say, >20 mm s^{-1}) [*Baldocchi et al.*, 1997]. Consequently, canopy transpiration calculated by BESS likely reflects the

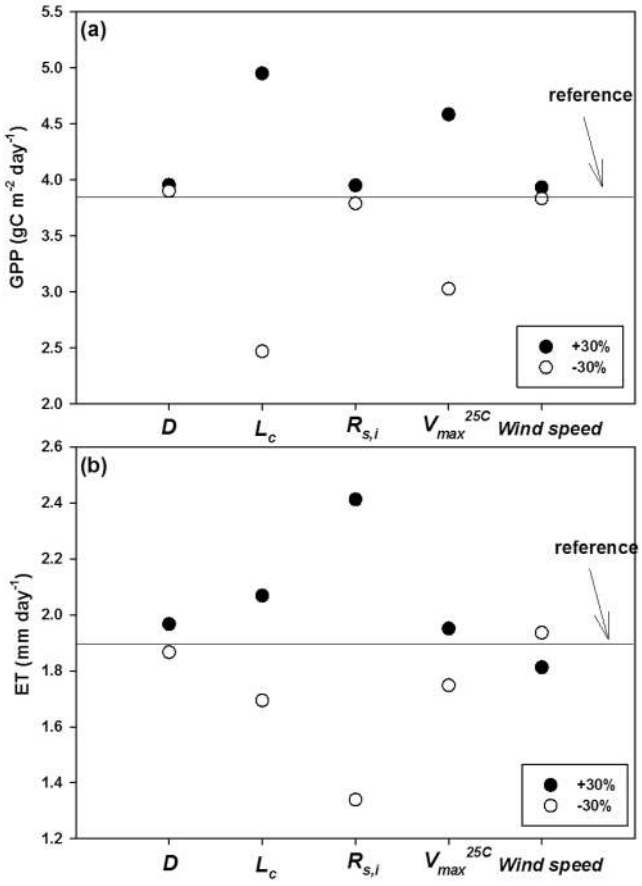

Figure 9. Sensitivity analysis of the BESS. Each variable was changed ±30%, and the output from the BESS for (a) gross primary productivity and (b) evapotranspiration was compared. *D*, vapor pressure deficit; L_c, leaf area index; $R_{s,I}$, incoming solar irradiance; V_{max}^{25C}, maximum carboxylation rate at 25C.

evaporation by the intercepted rainfall at least to some degree. These limitation in BESS model proved not to have a detrimental effect on the model performance, as the model seems to work well at a number of scales against measurements.

[60] We made BESS most sensitive to the variables that we can quantify reliably. We determined the variables as the atmospheric and canopy radiation components as it is possible to estimate incoming radiation and canopy structure variables such as leaf area index and clumping index from space. We found that BESS offered robust estimates of solar irradiance, except for the tropical regions that experienced intensive biomass burning (e.g., ID-Pag and AU-How sites) (Figures 3 and 6a). We believe the integration of atmosphere and sunlit-shade canopy radiative transfers at the same spatialc (1–5 km) and temporal (instantaneous) resolutions greatly reduced uncertainties related with nonlinear processes in canopy fluxes. Previous studies have illustrated scale-mismatches at both spatially (e.g., coarse resolution of solar irradiance with high resolution canopy properties) and temporally (e.g., use of daily to monthly mean solar irradiance) [*Fisher et al.*, 2008; *Mu et al.*, 2007; *Yuan et al.*, 2010; *Zhao et al.*, 2005]. Leaf area index was the most important variable that controlled canopy radiative transfer, and we found that the MODIS LAI was reliable at regional and seasonal scales although several important limitations were identified (see section 4.2). The clumping index that modifies canopy radiative transfer and the proportion of sunlit and shade leaves has been mostly ignored in global carbon and water flux studies even though field level studies have suggested the importance of clumping index in canopy modeling studies [*Baldocchi*, 1997; *Baldocchi et al.*, 2002, 1985; *Chen et al.*, 1999; *Norman and Jarvis*, 1974]. We compared the global GPP and ET between random canopy (clumping index = 1) and clumped canopy for the year 2002. The clumped canopy reduced GPP (1.5 PgC yr^{-1}) and increased ET (1,888 km^{-3} yr^{-1}) compared to the random canopy (Ω = 1). The difference in GPP was comparable to the carbon emissions caused by deforestation and forest degradation globally (1.2 PgC yr^{-1}) [*van der Werf et al.*, 2009] and caused by global transportation sector (1.7 PgC yr-1) [*Kahn Ribeiro et al.*, 2007], thus incorporating the foliar clumping effect into the carbon cycle model is important to reduce uncertainty in the global carbon cycle. The V_{max}^{25} was the second most important variable that controls GPP (Figure 9a). To estimate the values of V_{max}^{25}, we applied emerging ecological scaling rules that included the nitrogen concentration-albedo relationships [*Hollinger et al.*, 2010; *Ollinger et al.*, 2008] and the nitrogen concentration-leaf mass area relationships [*Reich et al.*, 1997; *Wright et al.*, 2004] for the closed canopy in boreal and temperate forests (see section 2.1.4). For the other land covers, we used the values of V_{max}^{25} from the literature survey by considering both climate zones and plant functional types (Table S2). Finally we applied seasonality of V_{max}^{25} which tends to reflect seasonal environmental stress [*Muraoka et al.*, 2010; *Wilson et al.*, 2001; *Xu and Baldocchi*, 2003]. We believe deducing $V_{max,tot}^{25C}$ by integrating the experimental evidences mentioned above enabled us to estimate GPP accurately.

[61] It has been reported that vapor pressure deficit from global reanalysis data introduced a major source of uncertainties in the MODIS GPP product [*Heinsch et al.*, 2006; *Zhao et al.*, 2006]. That was because the vapor pressure deficit directly controlled canopy conductance in the MODIS GPP algorithm. Physiologically, GPP is sensitive to both vapor pressure deficit and soil moisture availability to roots. For MODIS GPP, sensitivity to vapor pressure deficit was increased to represent moisture limitations to GPP because reliable data on the spatial water availability were not available. In BESS, we intended to avoid the dependence of GPP on the vapor pressure deficit by fixing the ratio of internal leaf and ambient CO_2 concentration (see section 2.1.4). In fact, BESS-derived GPP and ET were not highly sensitive to the vapor pressure deficit (Figure 9). *Zhao et al.* [2006] reported that different sources of coarse global reanalysis meteorological data could cause substantial differences (>20 PgC yr^{-1}) in the global GPP estimates based on the MODIS GPP algorithm. BESS avoided this issue by directly calculating meteorological variables from MODIS atmospheric products at high spatial resolution (1–5 km).

[62] The process-oriented approach enabled us to investigate what controls ET at the global scale (Figure 10). In situ data revealed that ET was highly correlated with net

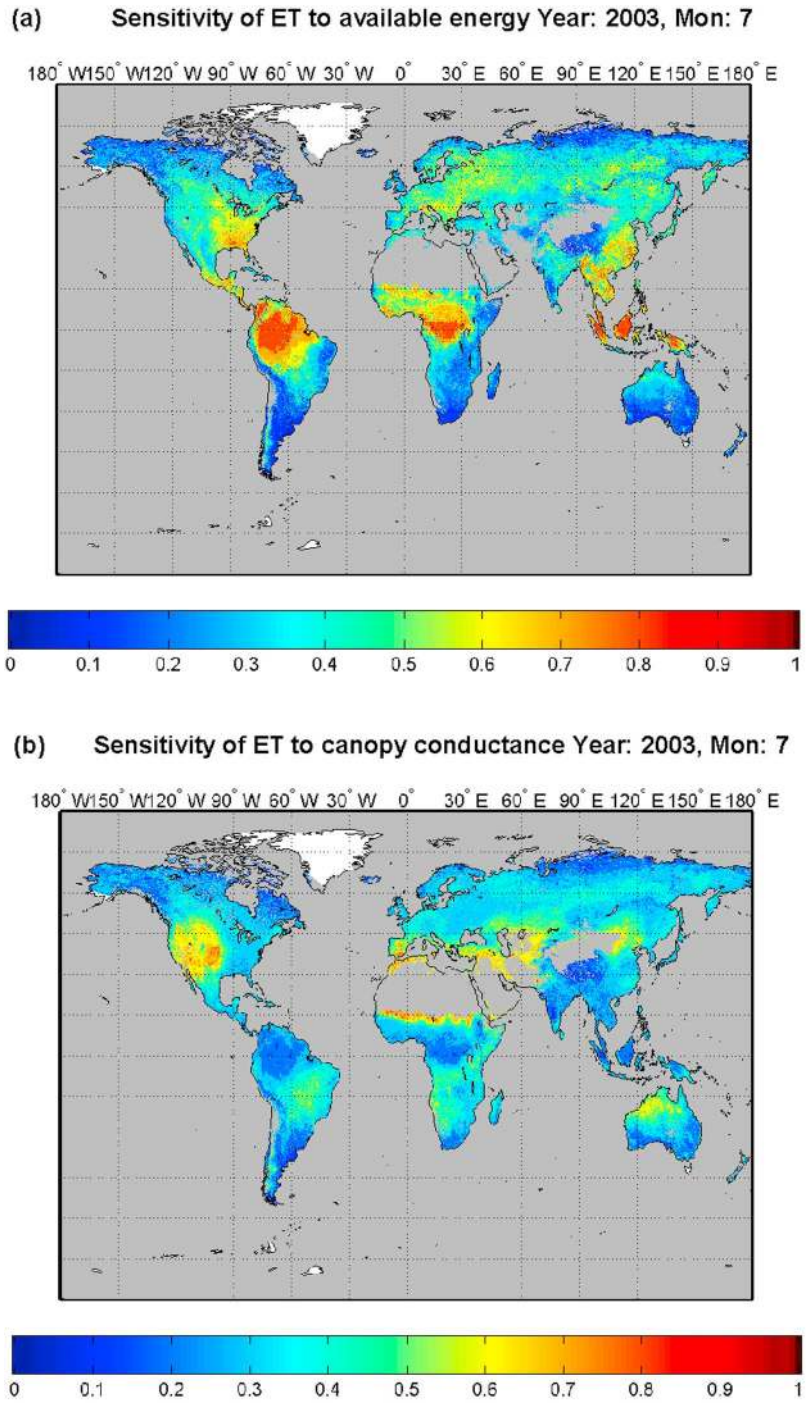

Figure 10. Global maps of sensitivity of ET to (a) available energy and (b) canopy conductance in July 2003. The sensitivity ranges between 0 (less sensitive) to 1 (positively highly sensitive). See section 2.7 for the calculation of the sensitivity.

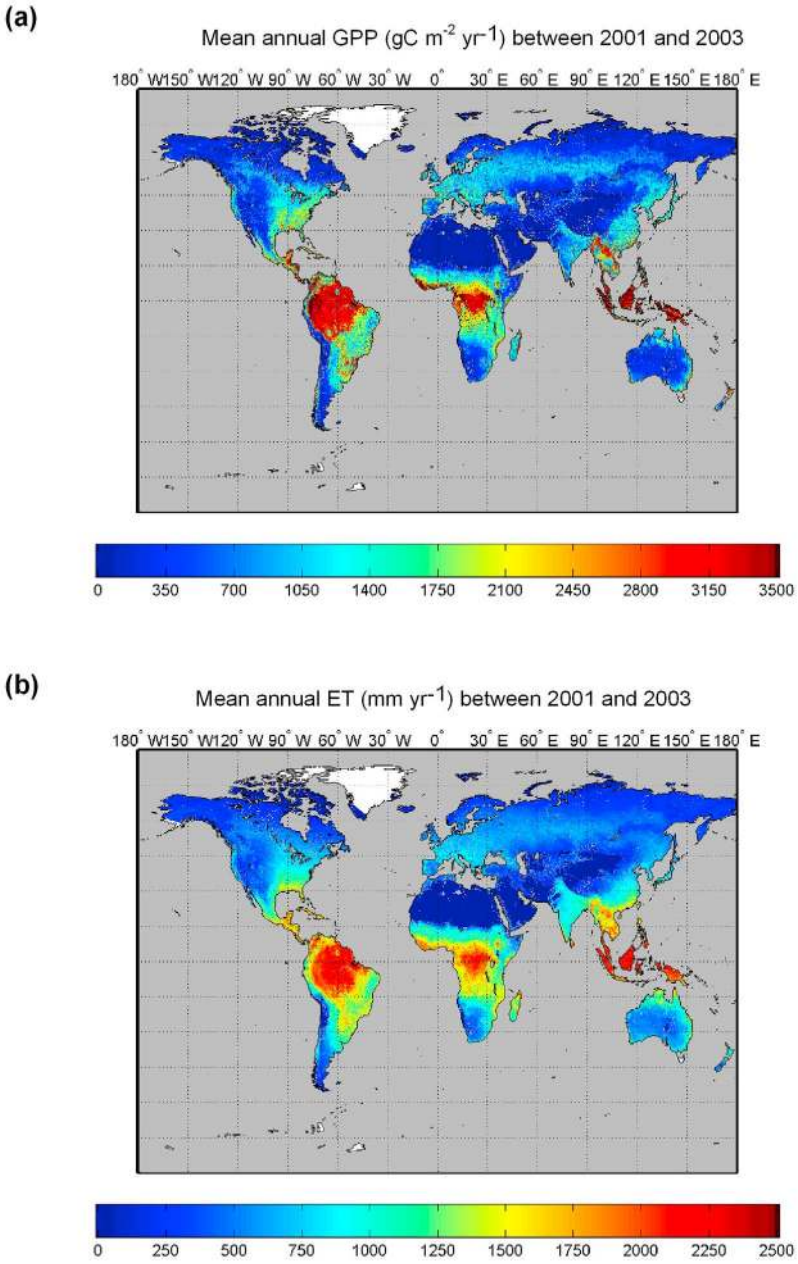

Figure 11. Global maps of (a) gross primary productivity and (b) evapotranspiration.

radiation in rain forests of Brazil whereas the correlation was less in southern Brazil due to water stress during the dry period [*Hasler and Avissar*, 2007]. This spatial gradient was well captured by BESS (Figure 10a). The sensitivity of ET to the available energy was positively high (>0.8) at the rain forests in Brazil and the sensitivity decreased along the southeast direction toward the cerrado, the tropical savanna ecoregion in Brazil. The sensitivity of ET to canopy conductance was fairly high (>0.5) in the cerrado region where dry winter season is pronounced between May and Oct.

4.2. Sources of Uncertainty in BESS

[63] The sensitivity analysis revealed that BESS-derived GPP was most sensitive to L_c (Figure 9). We found that inaccuracies in MODIS LAI led to major uncertainties at several sites. For example, the BESS showed substantial overestimation of GPP and ET at the AU-Tum site (see Figures 3 and 4). The peak L_c of MODIS LAI was twofold higher than the in situ L_c in this site (5 vs 2.5) [*Leuning et al.*, 2005; *Strahler et al.*, 2008]. It has also been reported that MODIS LAI overestimated L_c in eastern Australian open forests and woodlands [*Hill et al.*, 2006]. Next, seasonality of MODIS LAI for evergreen needleleaf forest types was exaggerated at most sites. For example, the in situ L_c in the Me2 site varied 2.6–3.5 over the year (Law, this study), but the MODIS LAI ranged 0–4. The MODIS LAI for the RU-Fyo site showed 0–4.8 over the year, but the field observation showed 2.5–3.5 over the year (A. Varlagin,

personal communication, 2010). The leaf area index of 0 in evergreen forests is unrealistic. The incorrect representation of phenology caused a simulated delay from BESS in the increase of GPP in the spring at the U.S.-Me2 and RU-Fyo sites. We found that the underestimated L_c during spring or autumn caused the underestimation of BESS-GPP in most evergreen needleleaf forest sites (Figure 4c). In the tropics, the selected MODIS LAI data that passed the quality check were few (see section 2.3.2) and provided a noisy signal and therefore a correction to L_c was unavoidable (i.e., keeping the peak L_c value over a 8-weeks period, see section 2.3.2). BESS-derived ET is coupled with GPP (equation (35)), and thus the uncertainty in GPP will be translated to uncertainties in ET. The sensitivity analysis revealed that BESS-derived ET was most sensitive to the $R_{s,i}$ (Figure 9b). Our $R_{s,i}$ model was generally reliable (relative RMSE and bias were 10% and 8%, respectively, see Figure 6a) although improvements were required in the tropics (see section 4.1); thus the uncertainty of L_c, which was the second most sensitive variable (Figure 9b), is likely to contribute a major source of uncertainty in the ET calculation. However, we note that the $R_{s,i}$ model in BESS overestimated R_s, during intensive biomass burning events in tropical forests (e.g., ID-Pag [*Hirano et al.*, 2007] and AU-How [*Kanniah et al.*, 2010]). We speculate that the characterization of aerosol properties used in the BESS needs improvement. Last, BESS did not consider complex terrain and heterogeneity of landscapes in a pixel, which might cause substantial biases in land surface radiation and energy balances [*Baldocchi et al.*, 2005; *Giorgi and Avissar*, 1997; *Ryu et al.*, 2008a]. We note that the uncertainty sources in input data and the gap-filling processes (see sections 2.3.1 and 2.3.2) can influence the results in the sensitivity analysis. In particular, a substantial data gap of MODIS data in the tropics and the way to fill the data gaps might impact the results in the sensitivity analysis substantially. We leave the detailed analysis on the impacts of the uncertainty sources on the sensitivity analysis for the next study.

4.3. Global Terrestrial Estimates of GPP and ET

[64] The global estimates of GPP and ET are still uncertain as reports varied between 107 and 167 PgC yr-1 [*Cramer et al.*, 2001; *Knorr and Heimann*, 2001], 123 PgC yr^{-1} [*Beer et al.*, 2010], 129 PgC yr^{-1} [*Demarty et al.*, 2007], 133 PgC yr^{-1} [*Ruimy et al.*, 1996], 109 PgC yr^{-1} [*Zhao et al.*, 2005], and 111 PgC yr^{-1} [*Yuan et al.*, 2010]. We quantified the mean global GPP between 2001 to 2003 as 118 ± 26 PgC yr^{-1}. Recently, *Beer et al.* [2010] quantified the global GPP as 123 ± 8 PgC yr^{-1} based on merging global flux tower data (i.e., "data-driven" approach). Interestingly, we found that BESS showed an excellent agreement with the *Beer et al.* (2010) across bioclimatic zones (Figure 7). Even if the two approaches were totally different (i.e., empirical vs process-based), they showed convergent estimates of global GPP. The global land ET is also highly uncertain [*Lettenmaier and Famiglietti*, 2006]. For example, a modeling study assumed a constant global land ET of 527 mm yr^{-1} without spatial and temporal variation of ET [*Wentz et al.*, 2007]. A range of global land ET was reported such as 613 mm yr^{-1} [*Fisher et al.*, 2008], 286 mm yr^{-1} [*Mu et al.*, 2007], 410 mm yr^{-1} [*Yuan et al.*, 2010], 550 mm yr^{-1} (65,000 km^3 yr^{-1}) [*Jung et al.*, 2010], and 539 mm yr^{-1} [*Zhang et al.*, 2010]. A recent ET synthesis study reported that the ensemble means of diagnostic models, land surface models, reanalysis models, IPCC AR4 models showed 606 mm yr^{-1}, 544 mm yr^{-1}, 631 mm yr^{-1} and 602 mm yr^{-1}, respectively [*Mueller et al.*, 2011]. Our global land ET estimate between 2001 and 2003 was 500 ± 104 mm yr^{-1} (equivalent to $63{,}000 \pm 13{,}100$ km^3 yr^{-1}). We note that our global ET estimate included deserts and alpine regions in Himalaya whereas some other studies only included vegetated land area which differs depending on the land cover product used. Thus reporting global ET as km^3 yr^{-1} unit is highly recommended to avoid any confusion. Our global ET estimate (63,000 km^2 yr^{-1}) was comparable from 65,000 km^2 yr^{-1} [*Jung et al.*, 2010] and 65,500 km^2 yr^{-1} [*Oki and Kanae*, 2006]. BESS-derived ET showed good agreement with the data-driven global ET product across bioclimatic zones and basin-level water balance ET [*Jung et al.*, 2010] (Figure 8). A systematic inter-comparison project across available GPP and ET models is warranted to identify where the models agree and disagree and how to improve them. The process-based BESS which couples two-leaf energy balance, canopy nitrogen, GPP and ET could offer mechanistic interpretation of the disagreement in the models, which is unlikely to be done in empirical approaches.

5. Summary and Conclusions

[65] In this study, we described and evaluated the mechanistic, coupled biophysical model, BESS. BESS coupled atmospheric and canopy radiative transfer processes, two-leaf photosynthesis, energy balance, and evapotranspiration using MODIS. The integration of biophysical processes with some assumptions that included soil water deficit is embedded inside the variations of leaf area index offered robust estimates of GPP and ET compared with the flux tower data, data-driven products, and basin-level water balance ET. Because we purposely increased sensitivity of BESS to leaf area index and solar irradiance, they were the most important variables that control GPP and ET, respectively. Over the three year period between 2001 and 2003, BESS quantified the global mean annual GPP and ET as 118 ± 26 PgC yr^{-1} and 500 ± 104 mm yr^{-1} (equivalent to $63{,}000 \pm 13{,}100$ km^3 yr^{-1}), respectively. BESS enabled us to investigate the sensitivity of ET to environmental and biological variables, which well captured the gradient of wetness from rain forests to seasonally drought forests in the Amazon. As BESS offers relatively high spatial resolution over the world (1- to 5-km resolution), we expect that BESS could be useful in local to the global applications such as climate research, water resources management, and identifying spots for solar harvesting.

Appendix A

[66] Appendix A includes the nomenclature and values used in this study. Table A1 includes symbols, their definitions, and if available, their values.

Table A1. Nomenclature and Values

Symbols	Definition	Value (or Derivation)
ρ_{cbP}	canopy reflectance for beam PAR	MODIS black-sky PAR albedo calculated with solar zenith angle and aerosol optical thickness
ρ_{cdP}	canopy reflectance for diffuse PAR	MODIS white-sky PAR albedo calculated with solar zenith angle and aerosol optical thickness
ρ_{cbN}	canopy reflectance for beam NIR	MODIS black-sky NIR albedo calculated with solar zenith angle and aerosol optical thickness
ρ_{cdN}	canopy reflectance for diffuse NIR	MODIS white-sky NIR albedo calculated with solar zenith angle and aerosol optical thickness
ρ_{sP}	soil reflectance for PAR	Table S1
ρ_{sN}	soil reflectance for NIR	Table S1
σ_{PAR}	leaf scattering coefficient for PAR	Table S1
σ_{NIR}	leaf scattering coefficient for NIR	Table S1
Q_{Pijk}	absorbed photosynthetically active radiation (μmol m^{-2} s^{-1}); $i = b$ for beam, and $i = d$ for diffuse; $j = Sun$ for sunlit leaf, and $j = Sh$ for shade leaf; $k = \downarrow$ for from sky to land direction, and $k = \uparrow$ for land to sky direction	equations (10) and (11)
Q_{Nijk}	absorbed NIR radiation (W m^{-2}); $i = b$ for beam, and $i = d$ for diffuse; $j = Sun$ for sunlit leaf, and $j = Sh$ for shade leaf; $k = \downarrow$ for from sky to land direction, and $k = \uparrow$ for land to sky direction	equations (18) and (19)
Q_{Lj}	absorbed longwave radiation (W m^{-2}); $j = Sun$ for sunlit leaf, and $j = Sh$ for shade leaf	equations (20) and (21)
α	shortwave albedo	MCD43B3 albedo calculated with solar zenith angle and aerosol optical thickness
$V_{max,\ j}^{25C}$	maximum carboxylation rate at 25C (μmol m^{-2} s^{-1}); $j = Sun$ for sunlit leaf, $j = Sh$ for shade leaf, and $j = tot$ for the entire canopy; no indication of j is leaf.	see section 2.1.4
$J_{max,j}^{25C}$	maximum electron transfer rate at 25C (μmol m^{-2} s^{-1}); $j = Sun$ for sunlit leaf, $j = Sh$ for shade leaf, and $j = tot$ for the entire canopy; no indication of j is leaf	see section 2.1.4
$A_{c,\ j}$	canopy photosynthesis; $j = Sun$ for sunlit leaf, and $j = Sh$ for shade leaf	equation (22)
$A_{l,\ j}$	light limited rate of CO_2 assimilation; $j = Sun$ for sunlit leaf, and $j = Sh$ for shade leaf	equation (23)
$A_{v,\ j}$	Rubisco limited rate of CO_2 assimilation; $j = Sun$ for sunlit leaf, and $j = Sh$ for shade leaf	equation (24)
$A_{s,\ j}$	capacity for the export or utilization of the products of photosynthesis for C3 species, and CO_2 limited flux for C4 species; $j = Sun$ for sunlit leaf, and $j = Sh$ for shade leaf	equation (25)
p_i	intercellular CO_2 partial pressure (Pa)	C3: $0.7 \times [CO2] \times 10^{-6} \times P$ and C4: $0.4 \times [CO2] \times 10^{-6} \times P$, where [CO2] is atmospheric CO2 concentration (370 ppm) and P is atmospheric pressure (Pa)
C_a	ambient atmospheric CO_2 concentration	370 ppm
P	atmospheric pressure (Pa)	MOD07
$\Gamma_{*,j}$	CO_2 compensation point of photosynthesis in the absence of mitochondrial respiration (Pa); $j = Sun$ for sunlit leaf, and $j = Sh$ for shade leaf	3.69 at 25C [*de Pury and Farquhar*, 1997]; see *de Pury and Farquhar* [1997, Table 4] to convert the value at the actual temperature
$K_{C,j}$	Michaelis-Menten constant of Rubisco for CO_2 (Pa)	40.4 at 25C [*de Pury and Farquhar*, 1997]; see *de Pury and Farquhar* [1997, Table 4] to convert the value at the actual temperature
$K_{O,j}$	Michaelis-Menten constant of Rubisco for O_2 (Pa)	24800 at 25C [*de Pury and Farquhar*, 1997]; see *de Pury and Farquhar* [1997, Table 4] to convert the value at the actual temperature
O	oxygen partial pressure (Pa)	20500 at 25C [*de Pury and Farquhar*, 1997]; see *de Pury and Farquhar* [1997, Table 4] to convert the value at the actual temperature
$R_{c,j}$	canopy respiration; $j = Sun$ for sunlit leaf, and $j = Sh$ for shade leaf	equation (26)
$E_a\_K_C$	activation energy for K_c	59400 [*de Pury and Farquhar*, 1997]
R	universal gas constant (J mol^{-1} K^{-1})	8.314
m	Ball-Berry slope (equation (35))	C3, 10; C4, 4
b	Ball-Berry offset (equation (35))	C3, 10^4 μmol m^{-2} s^{-1}; C4, 4×10^4 μmol m^{-2} s^{-1} [*Houborg et al.*, 2009]
r_a	aerodynamic resistance (s m^{-1})	NCEP wind speed; canopy height (Table S1)
$r_{c,j}$	canopy resistance for water vapor (s m^{-1}); $j = Sun$ for sunlit leaf, and $j = Sh$ for shade leaf	Ball-Berry equation (equation (35))
G_a	aerodynamic conductance (m s^{-1})	$1/r_a$
$G_{c,j}$	canopy conductance (m s^{-1}); $j = Sun$ for sunlit leaf, and $j = Sh$ for shade leaf	Ball-Berry equation (equation (35))
$N(\%)$	nitrogen concentration (mg g^{-1})	equation (27)
$N(area)$	nitrogen content (g m^{-2})	equation (29)
LMA	leaf mass per area (g m^{-2})	*Wright et al.* [2004]

Table A1. (continued)

Symbols	Definition	Value (or Derivation)
s	rate of change of saturation vapor pressure with air temperature (Pa K^{-1})	MOD07
γ	psychrometric constant (Pa K^{-1})	MOD07
λ	latent heat of vaporization (J kg^{-1})	MOD07
RH	relative humidity of the air (0–1)	MOD07
λE	latent heat flux (W m^{-2})	see section 2.1.6
σ	Stefan-Boltzmann constant (W m^{-2} K^{-4})	5.67×10^{-8}
ε_a	emissivity of the air	*Prata* [1996]
ε_l	emissivity of the leaf	0.98
ε_s	emissivity of the soil	0.94
c_p	specific heat of the air (J kg^{-1} K^{-1})	MOD07
ρ_a	air density (kg m^{-3})	MOD07
T_{Sun}	sunlit leaf temperature (K)	see section 2.1.5
T_{Sh}	shade leaf temperature (K)	see section 2.1.5
T_a	air temperature (K)	MOD07
D	vapor pressure deficit (Pa)	MOD07
g_r	radiative conductance (kg m^{-2} s^{-1})	$4\ \varepsilon_l\ \sigma T_a^3/c_p$
$e_s(T)$	saturated vapor pressure at temperature, T (Pa)	MOD07
$I_{P0}(L)$	total PAR radiation at canopy depth L (μmol m^{-2} s^{-1})	canopy radiative transfer model (see section 2.1.2)
$I_{Pb}(L)$	direct beam PAR at canopy depth L (μmol m^{-2} s^{-1})	canopy radiative transfer model (see section 2.1.2)
$I_{Pd}(L)$	diffuse PAR at canopy depth L (μmol m^{-2} s^{-1})	canopy radiative transfer model (see section 2.1.2)
$I_{N0}(L)$	total NIR radiation at canopy depth L (μmol m^{-2} s^{-1})	canopy radiative transfer model (see section 2.1.2)
$I_{Nb}(L)$	direct beam NIR at canopy depth L (μmol m^{-2} s^{-1})	canopy radiative transfer model (see section 2.1.2)
$I_{Nd}(L)$	diffuse NIR at canopy depth L (μmol m^{-2} s^{-1})	canopy radiative transfer model (see section 2.1.2)
$R_{s,i}$	incoming shortwave radiation above the canopy (W m^{-2})	atmospheric radiative transfer model (see section 2.1.1)
$R_{s,o}$	outgoing shortwave radiation above the canopy (W m^{-2})	atmospheric radiative transfer model and MCD43
$R_{l,i}$	incoming longwave radiation above the canopy (W m^{-2})	MOD07 and MOD05
$R_{l,o}$	outgoing longwave radiation above the canopy (W m^{-2})	MOD11
$R_{n,j}$	canopy net radiation (W m^{-2}); j = *Sun* for sunlit leaf, and j = *Sh* for shade leaf	atmospheric radiative transfer model, MCD43, MOD05, MOD07, and MOD11
$R_{n,soil}$	net radiation at soil surface (W m^{-2}).	equation (38)
R_n	sum net radiation of canopy and soil (W m^{-2}).	equation (38)
G_{soil}	soil heat flux (W m^{-2}).	equation (39)
R_{gPOT}	potential global solar irradiance (W m^{-2})	*Liu and Jordan* [1960]
θ	solar zenith angle at time of MODIS overpass	MOD06
Ω	foliar clumping index	global clumping index map
L	leaf area index (m^2 m^{-2})	MCD15
L_c	canopy leaf area index (m^2 m^{-2})	MCD15
G	projection coefficient of unit foliage area on a plane perpendicular to the view direction	0.5 (assuming spherical leaf inclination angle distribution)
$f_{sun}(L)$	the probability of leaf area being irradiated by direct beam at canopy depth L [*Gutschick*, 1991]	equation (1)
k	extinction coefficient (= $G(\theta)/\cos\theta$) assuming spherical leaf angle distribution	$0.5/\cos\theta$
k_b	extinction coefficient for beam PAR or NIR for black leaves	$0.5/\cos\theta$
k'_{Pb}	extinction coefficient for beam and scattered beam PAR	$0.46/\cos\theta$ [*de Pury and Farquhar*, 1997]
k'_{Pd}	extinction coefficient for diffuse and scattered diffuse PAR	0.72 [*de Pury and Farquhar*, 1997]
k'_{Nb}	extinction coefficient for beam and scattered beam NIR	equation (12)
k'_{Nd}	extinction coefficient for diffuse and scattered diffuse NIR	equation (13)
k'_L	extinction coefficient for longwave radiation	0.78 [*Goudriaan*, 1977]
k_n	nitrogen extinction coefficient	k'_{Pb}

[67] **Acknowledgments.** G. Farquhar and D. de Pury gave constructive comments on their model. Martin Jung, Christian Beer, Jan Pisek, and Jing Chen kindly shared their products. In particular, we thank Deb Agarwal, Keith Jackson and Marty Humphrey for their support on the use of Microsoft Azure Cloud Computing Service. Larry Flanagan, Russ Scott, Gil Bohrer, Andrej Varlagin, Tomomichi Kato, and Rodrigo Vargas gave constructive comments on the manuscript. Y.R. was supported by NASA Headquarters under the NASA Earth and Space Science Fellowship Program (NNX08AU25H) and the Berkeley Water Center/Microsoft eScience project, and supported by Korea-Americas Cooperation Program through the National Research Foundation of Korea (NRF) funded by the Korean Ministry of Education, Science and Technology (2011-0030485). MODIS data processing was supported by Microsoft Azure cloud computing service. Data from the Tonzi and Vaira Ranches was supported by the Office of Science (BER), U.S. Department of Energy, grant DE-FG02-06ER64308. This work used eddy covariance data acquired by the FLUXNET community and in particular by the following networks: AmeriFlux (U.S. Department of Energy, Biological and Environmental Research, Terrestrial Carbon Program (DE-FG02-04ER63917 and DE-FG02-04ER63911)), AfriFlux, AsiaFlux, CarboAfrica, CarboEuropeIP, CarboItaly, CarboMont, ChinaFlux, Fluxnet-Canada (supported by CFCAS, NSERC, BIOCAP, Environment Canada, and NRCan), GreenGrass, KoFlux, LBA, NECC, OzFlux, TCOS-Siberia, and USCCC. We acknowledge the financial support to the eddy covariance data harmonization provided by CarboEuropeIP, FAO-GTOS-TCO, iLEAPS, Max Planck Institute for Biogeochemistry, National Science Foundation, University of Tuscia, Universite Laval and Environment Canada and U.S. Department of Energy and the database development and technical support from Berkeley Water Center, Lawrence Berkeley National Laboratory, Microsoft Research eScience, Oak Ridge National Laboratory, University of California, Berkeley, and University of Virginia.

References

Agarwal, D., et al. (2011), Data-intensive science: The Terapixel and MODISAzure projects, *Int. J. High Perform. Comput. Appl.*, *25*(3), 304–316, doi:10.1177/1094342011414746.

Alton, P. B., R. Ellis, S. O. Los, and P. R. North (2007), Improved global simulations of gross primary product based on a separate and explicit treatment of diffuse and direct sunlight, *J. Geophys. Res.*, *112*, D07203, doi:10.1029/2006JD008022.

Anten, N. P. R., F. Schieving, and M. J. A. Werger (1995), Patterns Of light and nitrogen distribution in relation to whole canopy carbon gain in C-3 and C-4 monocotyledonous and dicotyledonous species, *Oecologia*, *101*(4), 504–513, doi:10.1007/BF00329431.

Asner, G. P., D. E. Knapp, A. N. Cooper, M. M. C. Bustamante, L. P. Olander, and K. B. Heidebrecht (2005), Ecosystem structure throughout the Brazilian Amazon from Landsat observations and automated spectral unmixing, *Earth Interact.*, *9*(7), 1–31, doi:10.1175/EI134.1.

Baldocchi, D. (1994), An analytical solution for coupled leaf photosynthesis and stomatal conductance models, *Tree Physiol.*, *14*(7–9), 1069–1079.

Baldocchi, D. (1997), Measuring and modelling carbon dioxide and water vapour exchange over a temperate broad-leaved forest during the 1995 summer drought, *Plant Cell Environ.*, *20*(9), 1108–1122, doi:10.1046/j.1365-3040.1997.d01-147.x.

Baldocchi, D., and T. Meyers (1998), On using eco-physiological, micrometeorological and biogeochemical theory to evaluate carbon dioxide, water vapor and trace gas fluxes over vegetation: A perspective, *Agric. For. Meteorol.*, *90*(1–2), 1–25, doi:10.1016/S0168-1923(97)00072-5.

Baldocchi, D. D., and K. B. Wilson (2001), Modeling CO_2 and water vapor exchange of a temperate broadleaved forest across hourly to decadal time scales, *Ecol. Modell.*, *142*(1–2), 155–184, doi:10.1016/S0304-3800(01)00287-3.

Baldocchi, D. D., D. R. Matt, B. A. Hutchison, and R. T. McMillen (1984), Solar radiation within an oak-hickory forest: An evaluation of the extinction coefficients for several radiation components during fully leafed and leafless periods, *Agric. For. Meteorol.*, *32*, 307–322, doi:10.1016/0168-1923(84)90056-X.

Baldocchi, D. D., B. A. Hutchison, D. R. Matt, and R. T. McMillen (1985), Canopy radiative transfer models for spherical and known leaf inclination angle distributions—A test in an oak hickory forest, *J. Appl. Ecol.*, *22*(2), 539–555, doi:10.2307/2403184.

Baldocchi, D. D., C. A. Vogel, and B. Hall (1997), Seasonal variation of energy and water vapor exchange rates above and below a boreal jack pine forest canopy, *J. Geophys. Res.*, *102*(D24), 28,939–28,951, doi:10.1029/96JD03325.

Baldocchi, D. D., B. E. Law, and P. M. Anthoni (2000), On measuring and modeling energy fluxes above the floor of a homogeneous and heterogeneous conifer forest, *Agric. For. Meteorol.*, *102*(2–3), 187–206, doi:10.1016/S0168-1923(00)00098-8.

Baldocchi, D. D., K. B. Wilson, and L. H. Gu (2002), How the environment, canopy structure and canopy physiological functioning influence carbon, water and energy fluxes of a temperate broad-leaved deciduous forest—An assessment with the biophysical model CANOAK, *Tree Physiol.*, *22*(15–16), 1065–1077.

Baldocchi, D. D., T. Krebs, and M. Y. Leclerc (2005), "Wet/dry Daisyworld": A conceptual tool for quantifying the spatial scaling of heterogeneous landscapes and its impact on the subgrid variability of energy fluxes, *Tellus, Ser. B*, *57*(3), 175–188, doi:10.1111/j.1600-0889.2005.00149.x.

Ball, J. T. (1988), An analysis of stomatal conductance, Ph.D. thesis, Stanford Univ., Palo Alto, Calif.

Beer, C., et al. (2010), Terrestrial gross carbon dioxide uptake: Global distribution and covariation with climate, *Science*, *329*(5993), 834–838, doi:10.1126/science.1184984.

Beven, K. (1979), Sensitivity analysis of the Penman-Monteith actual evapotranspiration estimates, *J. Hydrol.*, *44*(3–4), 169–190, doi:10.1016/0022-1694(79)90130-6.

Chen, J. M., J. Liu, J. Cihlar, and M. L. Goulden (1999), Daily canopy photosynthesis model through temporal and spatial scaling for remote sensing applications, *Ecol. Modell.*, *124*(2–3), 99–119, doi:10.1016/S0304-3800(99)00156-8.

Chen, J. M., C. H. Menges, and S. G. Leblanc (2005), Global mapping of foliage clumping index using multi-angular satellite data, *Remote Sens. Environ.*, *97*(4), 447–457, doi:10.1016/j.rse.2005.05.003.

Choudhury, B. J., S. B. Idso, and R. J. Reginato (1987), Analysis of an empirical-model for soil heat-flux under a growing wheat crop for estimating evaporation by an infrared-temperature based energy-balance equation, *Agric. For. Meteorol.*, *39*(4), 283–297, doi:10.1016/0168-1923(87)90021-9.

Ciais, P., et al. (2005), Europe-wide reduction in primary productivity caused by the heat and drought in 2003, *Nature*, *437*(7058), 529–533, doi:10.1038/nature03972.

Cleugh, H. A., R. Leuning, Q. Mu, and S. W. Running (2007), Regional evaporation estimates from flux tower and MODIS satellite data, *Remote Sens. Environ.*, *106*(3), 285–304, doi:10.1016/j.rse.2006.07.007.

Collatz, G. J., J. T. Ball, C. Grivet, and J. A. Berry (1991), Physiological and environmental regulation of stomatal conductance, photosynthesis and transpiration: A model that includes a laminar boundary layer, *Agric. For. Meteorol.*, *54*, 107–136, doi:10.1016/0168-1923(91)90002-8.

Collatz, G. J., M. Ribas-Carbo, and J. A. Berry (1992), Coupled photosynthesis-stomatal conductance model for leaves of C4 plants, *Aust. J. Plant Physiol.*, *19*(5), 519–538, doi:10.1071/PP9920519.

Cramer, W., et al. (2001), Global response of terrestrial ecosystem structure and function to CO_2 and climate change: Results from six dynamic global vegetation models, *Global Change Biol.*, *7*(4), 357–373, doi:10.1046/j.1365-2486.2001.00383.x.

Crawford, T. M., and C. E. Duchon (1999), An improved parameterization for estimating effective atmospheric emissivity for use in calculating daytime downwelling longwave radiation, *J. Appl. Meteorol.*, *38*(4), 474–480, doi:10.1175/1520-0450(1999)038<0474:AIPFEE>2.0.CO;2.

Dai, Y. J., R. E. Dickinson, and Y. P. Wang (2004), A two-big-leaf model for canopy temperature, photosynthesis, and stomatal conductance, *J. Clim.*, *17*(12), 2281–2299, doi:10.1175/1520-0442(2004)017<2281:ATMFCT>2.0.CO;2.

Demarty, J., F. Chevallier, A. D. Friend, N. Viovy, S. Piao, and P. Ciais (2007), Assimilation of global MODIS leaf area index retrievals within a terrestrial biosphere model, *Geophys. Res. Lett.*, *34*, L15402, doi:10.1029/2007GL030014.

de Pury, D. G. G., and G. D. Farquhar (1997), Simple scaling of photosynthesis from leaves to canopies without the errors of big-leaf models, *Plant Cell Environ.*, *20*(5), 537–557, doi:10.1111/j.1365-3040.1997.00094.x.

de Wit, C. T. (1970), Dynamic concepts in biology, in *Prediction and Measurement of Photosynthetic Productivity*, edited by I. Malek, pp. 17–23, Cent. for Agric. Publ. and Doc., Wageningen, Netherlands.

Fang, H., S. Liang, H. Y. Kim, J. R. Townshend, C. B. Schaaf, A. H. Strahler, and R. E. Dickinson (2007), Developing a spatially continuous 1 km surface albedo data set over North America from Terra MODIS products, *J. Geophys. Res.*, *112*, D20206, doi:10.1029/2006JD008377.

Fang, H., S. Liang, J. R. Townshend, and R. E. Dickinson (2008), Spatially and temporally continuous LAI data sets based on an integrated filtering method: Examples from North America, *Remote Sens. Environ.*, *112*, 75–93, doi:10.1016/j.rse.2006.07.026.

Farquhar, G. D., S. V. Caemmerer, and J. A. Berry (1980), A biochemical model of photosynthetic CO_2 assimilation in leaves of C_3 species, *Planta*, *149*(1), 78–90, doi:10.1007/BF00386231.

Fisher, J. B., K. P. Tu, and D. D. Baldocchi (2008), Global estimates of the land-atmosphere water flux based on monthly AVHRR and ISLSCP-II data, validated at 16 FLUXNET sites, *Remote Sens. Environ.*, *112*(3), 901–919, doi:10.1016/j.rse.2007.06.025.

Giorgi, F., and R. Avissar (1997), Representation of heterogeneity effects in earth system modeling: Experience from land surface modeling, *Rev. Geophys.*, *35*(4), 413–437, doi:10.1029/97RG01754.

Goudriaan, J. (1977), *Crop Micrometeorology: A Simulation Study*, Pudoc, Wageningen, Netherlands.

Gu, L. H., D. Baldocchi, S. B. Verma, T. A. Black, T. Vesala, E. M. Falge, and P. R. Dowty (2002), Advantages of diffuse radiation for terrestrial ecosystem productivity, *J. Geophys. Res.*, *107*(D6), 4050, doi:10.1029/2001JD001242.

Gutschick, V. P. (1991), Joining leaf photosynthesis models and canopy photon-transport models, in *Photon-Vegetation Interaction: Applications in Optical Remote Sensing and Plant Ecology*, edited by R. B. Myneni and J. Ross, pp. 501–535, Springer, Berlin.

Hanan, N. P., J. A. Berry, S. B. Verma, E. A. Walter-Shea, A. E. Suyker, G. G. Burba, and A. S. Denning (2005), Testing a model of CO_2, water and energy exchange in Great Plains tallgrass prairie and wheat ecosystems, *Agric. For. Meteorol.*, *131*(3–4), 162–179, doi:10.1016/j.agrformet.2005.05.009.

Harley, P. C., and D. D. Baldocchi (1995), Scaling carbon-dioxide and water-vapor exchange from leaf to canopy in a deciduous forest. 1. Leaf model parametrization, *Plant Cell Environ.*, *18*(10), 1146–1156, doi:10.1111/j.1365-3040.1995.tb00625.x.

Harley, P. C., R. B. Thomas, J. F. Reynolds, and B. R. Strain (1992), Modelling photosynthesis of cotton grown in elevated CO_2, *Plant Cell Environ.*, *15*(3), 271–282, doi:10.1111/j.1365-3040.1992.tb00974.x.

Hasler, N., and R. Avissar (2007), What controls evapotranspiration in the Amazon Basin?, *J. Hydrometeorol.*, *8*(3), 380–395, doi:10.1175/JHM587.1.

Heinsch, F. A., et al. (2006), Evaluation of remote sensing based terrestrial productivity from MODIS using regional tower eddy flux network observations, *IEEE Trans. Geosci. Remote Sens.*, *44*(7), 1908–1925, doi:10.1109/TGRS.2005.853936.

Henderson-Sellers, B. (1984), A new formula for latent heat of vaporization of water as a function of temperature, *Q. J. R. Meteorol. Soc.*, *110*(466), 1186–1190, doi:10.1002/qj.49711046626.

Hess, M., P. Koepke, and I. Schult (1998), Optical properties of aerosols and clouds: The software package OPAC, *Bull. Am. Meteorol. Soc.*,

79(5), 831–844, doi:10.1175/1520-0477(1998)079<0831:OPOAAC>2.0.CO;2.

Hikosaka, K. (2003), A model of dynamics of leaves and nitrogen in a plant canopy: An integration of canopy photosynthesis, leaf life span, and nitrogen use efficiency, *Am. Nat.*, *162*(2), 149–164, doi:10.1086/376576.

Hikosaka, K., E. Nabeshima, and T. Hiura (2007), Seasonal changes in the temperature response of photosynthesis in canopy leaves of Quercus crispula in a cool-temperate forest, *Tree Physiol.*, *27*(7), 1035–1041.

Hilker, T., A. Lyapustin, F. G. Hall, Y. Wang, N. C. Coops, G. Drolet, and T. A. Black (2009), An assessment of photosynthetic light use efficiency from space: Modeling the atmospheric and directional impacts on PRI reflectance, *Remote Sens. Environ.*, *113*(11), 2463–2475, doi:10.1016/j.rse.2009.07.012.

Hill, M. J., U. Senarath, A. Lee, M. Zeppel, J. M. Nightingale, R. D. J. Williams, and T. R. McVicar (2006), Assessment of the MODIS LAI product for Australian ecosystems, *Remote Sens. Environ.*, *101*(4), 495–518, doi:10.1016/j.rse.2006.01.010.

Hirano, T., H. Segah, T. Harada, S. Limin, T. June, R. Hirata, and M. Osaki (2007), Carbon dioxide balance of a tropical peat swamp forest in Kalimantan, Indonesia, *Global Change Biol.*, *13*(2), 412–425, doi:10.1111/j.1365-2486.2006.01301.x.

Hollinger, D. Y., et al. (2010), Albedo estimates for land surface models and support for a new paradigm based on foliage nitrogen concentration, *Global Change Biol.*, *16*(2), 696–710, doi:10.1111/j.1365-2486.2009.02028.x.

Houborg, R., H. Soegaard, W. Emmerich, and S. Moran (2007), Inferences of all-sky solar irradiance using Terra and Aqua MODIS satellite data, *Int. J. Remote Sens.*, *28*(20), 4509–4535, doi:10.1080/01431160701241902.

Houborg, R., M. C. Anderson, J. M. Norman, T. Wilson, and T. Meyers (2009), Intercomparison of a 'bottom-up' and 'top-down' modeling paradigm for estimating carbon and energy fluxes over a variety of vegetative regimes across the U.S., *Agric. For. Meteorol.*, *149*(11), 1875–1895, doi:10.1016/j.agrformet.2009.06.014.

Hua, X. M., J. F. Pan, D. Ouzounov, A. Lyapustin, Y. J. Wang, K. Tewari, G. Leptoukh, and B. Vollmer (2007), A spatial prescreening technique for earth observation data, *IEEE Geosci. Remote Sens. Lett.*, *4*(1), 152–156, doi:10.1109/LGRS.2006.886421.

Huete, A. R., N. Restrepo-Coupe, P. Ratana, K. Didan, S. R. Saleska, K. Ichii, S. Panuthai, and M. Gamo (2008), Multiple site tower flux and remote sensing comparisons of tropical forest dynamics in Monsoon Asia, *Agric. For. Meteorol.*, *148*(5), 748–760, doi:10.1016/j.agrformet.2008.01.012.

Iwabuchi, H. (2006), Efficient Monte Carlo methods for radiative transfer modeling, *J. Atmos. Sci.*, *63*(9), 2324–2339, doi:10.1175/JAS3755.1.

Jarvis, P. G. (1995), Scaling processes and problems, *Plant Cell Environ.*, *18*(10), 1079–1089, doi:10.1111/j.1365-3040.1995.tb00620.x.

Jones, H. G. (1992), *Plants and Microclimate: A Quantitative Approach to Environmental Plant Physiology*, Cambridge Univ. Press, Cambridge, U. K.

Jung, M., M. Reichstein, and A. Bondeau (2009), Towards global empirical upscaling of FLUXNET eddy covariance observations: Validation of a model tree ensemble approach using a biosphere model, *Biogeosciences*, *6*(10), 2001–2013, doi:10.5194/bg-6-2001-2009.

Jung, M., et al. (2010), Recent decline in the global land evapotranspiration trend due to limited moisture supply, *Nature*, *467*(7318), 951–954, doi:10.1038/nature09396.

Kahn Ribeiro, S., et al. (2007), *Transport and Its Infrastructure*, Cambridge Univ. Press, Cambridge, U. K.

Kalnay, E., et al. (1996), The NCEP/NCAR 40-year reanalysis project, *Bull. Am. Meteorol. Soc.*, *77*(3), 437–471, doi:10.1175/1520-0477(1996)077<0437:TNYRP>2.0.CO;2.

Kanniah, K. D., J. Beringer, N. J. Tapper, and C. N. Long (2010), Aerosols and their influence on radiation partitioning and savanna productivity in northern Australia, *Theor. Appl. Climatol.*, *100*(3–4), 423–438, doi:10.1007/s00704-009-0192-z.

Kattge, J., and W. Knorr (2007), Temperature acclimation in a biochemical model of photosynthesis: A reanalysis of data from 36 species, *Plant Cell Environ.*, *30*(9), 1176–1190, doi:10.1111/j.1365-3040.2007.01690.x.

Kattge, J., W. Knorr, T. Raddatz, and C. Wirth (2009), Quantifying photosynthetic capacity and its relationship to leaf nitrogen content for global-scale terrestrial biosphere models, *Global Change Biol.*, *15*, 976–991, doi:10.1111/j.1365-2486.2008.01744.x.

Key, J. R., and A. J. Schweiger (1998), Tools for atmospheric radiative transfer: Streamer and FluxNet, *Comput. Geosci.*, *24*(5), 443–451, doi:10.1016/S0098-3004(97)00130-1.

Knorr, W., and M. Heimann (2001), Uncertainties in global terrestrial biosphere modeling: 1. A comprehensive sensitivity analysis with a new photosynthesis and energy balance scheme, *Global Biogeochem. Cycles*, *15*(1), 207–225, doi:10.1029/1998GB001059.

Kobayashi, H., and H. Iwabuchi (2008), A coupled 1-D atmosphere and 3-D canopy radiative transfer model for canopy reflectance, light environment, and photosynthesis simulation in a heterogeneous landscape, *Remote Sens. Environ.*, *112*(1), 173–185, doi:10.1016/j.rse.2007.04.010.

Konecny, G. (1979), Methods and possibilities for digital differential rectification, *Photogramm. Eng. Remote Sens.*, *45*(6), 727–734.

Kosugi, Y., S. Shibata, and S. Kobashi (2003), Parameterization of the CO_2 and H_2O gas exchange of several temperate deciduous broad-leaved trees at the leaf scale considering seasonal changes, *Plant Cell Environ.*, *26*(2), 285–301, doi:10.1046/j.1365-3040.2003.00960.x.

Kottek, M., J. Grieser, C. Beck, B. Rudolf, and F. Rubel (2006), World map of the Koppen-Geiger climate classification updated, *Meteorol. Z.*, *15*(3), 259–263, doi:10.1127/0941-2948/2006/0130.

Law, B. E., A. Cescatti, and D. D. Baldocchi (2001), Leaf area distribution and radiative transfer in open-canopy forests: Implications for mass and energy exchange, *Tree Physiol.*, *21*, 777–787.

Lee, Y. H., and L. Mahrt (2004), Comparison of heat and moisture fluxes from a modified soil-plant-atmosphere model with observations from BOREAS, *J. Geophys. Res.*, *109*, D08103, doi:10.1029/2003JD003949.

Lemeur, R., and B. L. Blad (1974), A critical review of light models for estimating the shortwave radiation regime of plant canopies, *Agric. Meteorol.*, *14*(1–2), 255–286, doi:10.1016/0002-1571(74)90024-7.

Lettenmaier, D. P., and J. S. Famiglietti (2006), Water from on high, *Nature*, *444*(7119), 562–563, doi:10.1038/444562a.

Leuning, R., F. M. Kelliher, D. G. G. de Pury, and E. D. Schulze (1995), Leaf nitrogen, photosynthesis, conductance and transpiration—Scaling from leaves to canopies, *Plant Cell Environ.*, *18*(10), 1183–1200, doi:10.1111/j.1365-3040.1995.tb00628.x.

Leuning, R., H. A. Cleugh, S. J. Zegelin, and D. Hughes (2005), Carbon and water fluxes over a temperate Eucalyptus forest and a tropical wet/dry savanna in Australia: Measurements and comparison with MODIS remote sensing estimates, *Agric. For. Meteorol.*, *129*, 151–173, doi:10.1016/j.agrformet.2004.12.004.

Li, J., M. Humphrey, D. Agarwal, K. Jackson, C. van Ingen, and Y. Ryu (2010), eScience in the cloud: A MODIS satellite data reprojection and reduction pipeline in the Windows Azure platform, paper presented at International Parallel and Distributed Processing Symposium, Inst. of Electr. and Electron. Eng., Atlanta, Ga., 19–23 April.

Liang, S. L., T. Zheng, R. G. Liu, H. L. Fang, S. C. Tsay, and S. Running (2006), Estimation of incident photosynthetically active radiation from Moderate Resolution Imaging Spectrometer data, *J. Geophys. Res.*, *111*, D15208, doi:10.1029/2005JD006730.

Limousin, J.-M., L. Misson, A.-V. Lavoir, N. K. Martin, and S. Rambal (2010), Do photosynthetic limitations of evergreen *Quercus ilex* leaves change with long-term increased drought severity?, *Plant Cell Environ.*, *33*, 863–875.

Liu, B. Y. H., and R. C. Jordan (1960), The interrelationship and characteristic distribution of direct, diffuse and total solar radiation, *Sol. Energy*, *4*(3), 1–19, doi:10.1016/0038-092X(60)90062-1.

Martin, S. T., et al. (2010), Sources and properties of Amazonian aerosol particles, *Rev. Geophys.*, *48*, RG2002, doi:10.1029/2008RG000280.

McCabe, M. F., E. F. Wood, R. Wojcik, M. Pan, J. Sheffield, H. Gao, and H. Su (2008), Hydrological consistency using multi-sensor remote sensing data for water and energy cycle studies, *Remote Sens. Environ.*, *112*(2), 430–444, doi:10.1016/j.rse.2007.03.027.

McCuen, R. H. (1974), A sensitivity and error analysis of procedures used for estimating evaporation, *J. Am. Water Resour. Assoc.*, *10*(3), 486–497, doi:10.1111/j.1752-1688.1974.tb00590.x.

Michalsky, J. J. (1988), The astronomical-almanacs algorithm for approximate solar position (1950–2050), *Sol. Energy*, *40*(3), 227–235, doi:10.1016/0038-092X(88)90045-X.

Miralles, D. G., J. H. Gash, T. R. H. Holmes, R. A. M. de Jeu, and A. J. Dolman (2010), Global canopy interception from satellite observations, *J. Geophys. Res.*, *115*, D16122, doi:10.1029/2009JD013530.

Monteith, J. L. (1965), Evaporation and the environment, *Symp. Soc. Explor. Biol.*, *19*, 205–234.

Mu, Q., F. A. Heinsch, M. Zhao, and S. W. Running (2007), Development of a global evapotranspiration algorithm based on MODIS and global meteorology data, *Remote Sens. Environ.*, *111*(4), 519–536, doi:10.1016/j.rse.2007.04.015.

Mueller, B., et al. (2011), Evaluation of global observations-based evapotranspiration datasets and IPCC AR4 simulations, *Geophys. Res. Lett.*, *38*, L06402, doi:10.1029/2010GL046230.

Muraoka, H., N. Saigusa, K. N. Nasahara, H. Noda, J. Yoshino, T. M. Saitoh, S. Nagai, S. Murayama, and H. Koizumi (2010), Effects of seasonal and interannual variations in leaf photosynthesis and canopy leaf area index on gross primary production of a cool-temperate deciduous

broadleaf forest in Takayama, Japan, *J. Plant Res.*, *123*(4), 563–576, doi:10.1007/s10265-009-0270-4.

Norman, J. M. (1982), Simulation of microclimates, in *Biometeorology in Integrated Pest Management*, edited by J. L. Hatfield and I. J. Thomason, pp. 65–100, Academic, San Diego, Calif.

Norman, J. M., and P. G. Jarvis (1974), Photosynthesis in sitka spruce (*Picea-sitchensis* (Bong) carr) 3. Measurements of canopy structure and interception of radiation, *J. Appl. Ecol.*, *11*(1), 375–398, doi:10.2307/2402028.

Norman, J. M., and P. G. Jarvis (1975), Photosynthesis in Sitka Spruce (*Picea-Sitchensis* (Bong) Carr). 5. Radiation penetration theory and a test case, *J. Appl. Ecol.*, *12*(3), 839–878, doi:10.2307/2402094.

Norman, J. M., W. P. Kustas, and K. S. Humes (1995), Source approach for estimating soil and vegetation energy fluxes in observations of directional radiometric surface temperature, *Agric. For. Meteorol.*, *77*(3–4), 263–293, doi:10.1016/0168-1923(95)02265-Y.

Oki, T., and S. Kanae (2006), Global hydrological cycles and world water resources, *Science*, *313*(5790), 1068–1072, doi:10.1126/science.1128845.

Ollinger, S. V., et al. (2008), Canopy nitrogen, carbon assimilation, and albedo in temperate and boreal forests: Functional relations and potential climate feedbacks, *Proc. Natl. Acad. Sci. U. S. A.*, *105*(49), 19,336–19,341, doi:10.1073/pnas.0810021105.

Osmond, C. B., O. Björkman, and D. J. Anderson (1980), *Physiological Processes in Plant Ecology: Towards a Synthesis With Atriplex*, Springer, Berlin.

Paw U K. T., and W. G. Gao (1988), Applications of solutions to non-linear energy budget equations, *Agric. For. Meteorol.*, *43*(2), 121–145, doi:10.1016/0168-1923(88)90087-1.

Pisek, J., J. M. Chen, R. Lacaze, O. Sonnentag, and K. Alikas (2010), Expanding global mapping of the foliage clumping index with multi-angular POLDER three measurements: Evaluation and topographic compensation, *ISPRS J. Photogramm. Remote Sens.*, *65*(4), 341–346, doi:10.1016/j.isprsjprs.2010.03.002.

Prata, A. J. (1996), A new long-wave formula for estimating downward clear-sky radiation at the surface, *Q. J. R. Meteorol. Soc.*, *122*(533), 1127–1151, doi:10.1002/qj.49712253306.

Priestley, C. H. B., and R. J. Taylor (1972), On the assessment of surface heat flux and evaporation using large-scale parameters, *Mon. Weather Rev.*, *100*(2), 81–92, doi:10.1175/1520-0493(1972)100<0081:OTAOSH>2.3.CO;2.

Rambal, S., J. M. Ourcival, R. Joffre, F. Mouillot, Y. Nouvellon, M. Reichstein, and A. Rocheteau (2003), Drought controls over conductance and assimilation of a Mediterranean evergreen ecosystem: Scaling from leaf to canopy, *Global Change Biol.*, *9*(12), 1813–1824, doi:10.1111/j.1365-2486.2003.00687.x.

Reich, P. B., M. B. Walters, and D. S. Ellsworth (1997), From tropics to tundra: Global convergence in plant functioning, *Proc. Natl. Acad. Sci. U. S. A.*, *94*(25), 13,730–13,734, doi:10.1073/pnas.94.25.13730.

Reichstein, M., J. Tenhunen, O. Roupsard, J. M. Ourcival, S. Rambal, F. Miglietta, A. Peressotti, M. Pecchiari, G. Tirone, and R. Valentini (2003), Inverse modeling of seasonal drought effects on canopy CO2/H2O exchange in three Mediterranean ecosystems, *J. Geophys. Res.*, *108*(D23), 4726, doi:10.1029/2003JD003430.

Reichstein, M., et al. (2005), On the separation of net ecosystem exchange into assimilation and ecosystem respiration: Review and improved algorithm, *Global Change Biol.*, *11*(9), 1424–1439, doi:10.1111/j.1365-2486.2005.001002.x.

Rodell, M., J. S. Famiglietti, J. Chen, S. I. Seneviratne, P. Viterbo, S. Holl, and C. R. Wilson (2004), Basin scale estimates of evapotranspiration using GRACE and other observations, *Geophys. Res. Lett.*, *31*, L20504, doi:10.1029/2004GL020873.

Ruimy, A., G. Dedieu, and B. Saugier (1996), TURC: A diagnostic model of continental gross primary productivity and net primary productivity, *Global Biogeochem. Cycles*, *10*(2), 269–285, doi:10.1029/96GB00349.

Running, S. W., R. R. Nemani, F. A. Heinsch, M. S. Zhao, M. Reeves, and H. Hashimoto (2004), A continuous satellite-derived measure of global terrestrial primary production, *Bioscience*, *54*(6), 547–560, doi:10.1641/0006-3568(2004)054[0547:ACSMOG]2.0.CO;2.

Ryu, Y., S. Kang, S. K. Moon, and J. Kim (2008a), Evaluation of land surface radiation balance derived from Moderate Resolution Imaging Spectrometer (MODIS) over complex terrain and heterogeneous landscape on clear sky days, *Agric. For. Meteorol.*, *148*(10), 1538–1552, doi:10.1016/j.agrformet.2008.05.008.

Ryu, Y., D. D. Baldocchi, S. Ma, and T. Hehn (2008b), Interannual variability of evapotranspiration and energy exchanges over an annual grassland in California, *J. Geophys. Res.*, *113*, D09104, doi:10.1029/2007JD009263.

Ryu, Y., T. Nilson, H. Kobayashi, O. Sonnentag, B. E. Law, and D. D. Baldocchi (2010a), On the correct estimation of effective leaf area index: Does it reveal information on clumping effects?, *Agric. For. Meteorol.*, *150*(3), 463–472, doi:10.1016/j.agrformet.2010.01.009.

Ryu, Y., O. Sonnentag, T. Nilson, R. Vargas, H. Kobayashi, R. Wenk, and D. D. Baldocchi (2010b), How to quantify tree leaf area index in a heterogeneous savanna ecosystem: A multi-instrument and multi-model approach, *Agric. For. Meteorol.*, *150*(1), 63–76, doi:10.1016/j.agrformet.2009.08.007.

Ryu, Y., D. D. Baldocchi, J. Verfaillie, S. Ma, M. Falk, I. Ruiz-Mercado, T. Hehn, and O. Sonnentag (2010c), Testing the performance of a novel spectral reflectance sensor, built with light emitting diodes (LEDs), to monitor ecosystem metabolism, structure and function, *Agric. For. Meteorol.*, *150*(12), 1597–1606, doi:10.1016/j.agrformet.2010.08.009.

Ryu, Y., et al. (2012), On the temporal upscaling of evapotranspiration from instantaneous remote sensing measurements to 8-day mean daily sums, *Agric. For. Meteorol.*, *152*, 212–222, doi:10.1016/j.agrformet.2011.09.010.

Schulze, E. D., F. M. Kelliher, C. Korner, J. Lloyd, and R. Leuning (1994), Relationships among maximum stomatal conductance, ecosystem surface conductance, carbon assimilation rate, and plant nitrogen nutrition—A global ecology scaling exercise, *Annu. Rev. Ecol. Syst.*, *25*, 629–662, doi:10.1146/annurev.es.25.110194.003213.

Scott, R. L., E. P. Hamerlynck, G. D. Jenerette, M. S. Moran, and G. A. Barron-Gafford (2010), Carbon dioxide exchange in a semidesert grassland through drought-induced vegetation change, *J. Geophys. Res.*, *115*, G03026, doi:10.1029/2010JG001348.

Sims, D. A., et al. (2008), A new model of gross primary productivity for North American ecosystems based solely on the enhanced vegetation index and land surface temperature from MODIS, *Remote Sens. Environ.*, *112*, 1633–1646, doi:10.1016/j.rse.2007.08.004.

Sinclair, T. R., C. E. Murphy, and K. R. Knoerr (1976), Development and evaluation of simplified models for simulating canopy photosynthesis and transpiration, *J. Appl. Ecol.*, *13*(3), 813–829, doi:10.2307/2402257.

Still, C. J., J. A. Berry, G. J. Collatz, and R. S. DeFries (2003), Global distribution of C3 and C4 vegetation: Carbon cycle implications, *Global Biogeochem. Cycles*, *17*(1), 1006, doi:10.1029/2001GB001807.

Strahler, A. H., et al. (2008), Retrieval of forest structural parameters using a ground-based lidar instrument (Echidna (R)), *Can. J. Rem. Sens.*, *34*, S426–S440, doi:10.5589/m08-046.

Su, Z. (2002), The Surface Energy Balance System (SEBS) for estimation of turbulent heat fluxes, *Hydrol. Earth Syst. Sci.*, *6*(1), 85–100, doi:10.5194/hess-6-85-2002.

Thomas, C. K., B. E. Law, J. Irvine, J. G. Martin, J. C. Pettijohn, and K. J. Davis (2009), Seasonal hydrology explains interannual and seasonal variation in carbon and water exchange in a semiarid mature ponderosa pine forest in central Oregon, *J. Geophys. Res.*, *114*, G04006, doi:10.1029/2009JG001010.

van der Werf, G. R., D. C. Morton, R. S. DeFries, J. G. J. Olivier, P. S. Kasibhatla, R. B. Jackson, G. J. Collatz, and J. T. Randerson (2009), CO2 emissions from forest loss, *Nat. Geosci.*, *2*(11), 737–738, doi:10.1038/ngeo671.

Van Laake, P. E., and G. A. Sanchez-Azofeifa (2004), Simplified atmospheric radiative transfer modelling for estimating incident PAR using MODIS atmosphere products, *Remote Sens. Environ.*, *91*(1), 98–113, doi:10.1016/j.rse.2004.03.002.

Vermote, E. F., D. Tanre, J. L. Deuze, M. Herman, and J. J. Morcrette (1997), Second Simulation of the Satellite Signal in the Solar Spectrum, 6S: An overview, *IEEE Trans. Geosci. Remote Sens.*, *35*(3), 675–686, doi:10.1109/36.581987.

Wang, Q., A. Iio, J. Tenhunen, and Y. Kakubari (2008), Annual and seasonal variations in photosynthetic capacity of Fagus crenata along an elevation gradient in the Naeba Mountains, Japan, *Tree Physiol.*, *28*(2), 277–285.

Wang, Y.-P., and R. Leuning (1998), A two-leaf model for canopy conductance, photosynthesis and partitioning of available energy I: Model description and comparison with a multi-layered model, *Agric. For. Meteorol.*, *91*, 89–111, doi:10.1016/S0168-1923(98)00061-6.

Wang, Y. P., D. Baldocchi, R. Leuning, E. Falge, and T. Vesala (2007), Estimating parameters in a land-surface model by applying nonlinear inversion to eddy covariance flux measurements from eight FLUXNET sites, *Global Change Biol.*, *13*(3), 652–670, doi:10.1111/j.1365-2486.2006.01225.x.

Wentz, F. J., L. Ricciardulli, K. Hilburn, and C. Mears (2007), How much more rain will global warming bring?, *Science*, *317*(5835), 233–235, doi:10.1126/science.1140746.

Wilson, K. B., P. J. Hanson, and D. D. Baldocchi (2000), Factors controlling evaporation and energy partitioning beneath a deciduous forest over an annual cycle, *Agric. For. Meteorol.*, *102*(2–3), 83–103, doi:10.1016/S0168-1923(00)00124-6.

Wilson, K. B., D. D. Baldocchi, and P. J. Hanson (2001), Leaf age affects the seasonal pattern of photosynthetic capacity and net ecosystem exchange of carbon in a deciduous forest, *Plant Cell Environ.*, *24*(6), 571–583, doi:10.1046/j.0016-8025.2001.00706.x.

Wolfe, R. E., D. P. Roy, and E. Vermote (1998), MODIS land data storage, gridding, and compositing methodology: Level 2 grid, *IEEE Trans. Geosci. Remote Sens.*, *36*(4), 1324–1338, doi:10.1109/36.701082.

Wong, S. C., I. R. Cowan, and G. D. Farquhar (1979), Stomatal conductance correlates with photosynthetic capacity, *Nature*, *282*(5737), 424–426, doi:10.1038/282424a0.

Wright, I. J., et al. (2004), The worldwide leaf economics spectrum, *Nature*, *428*(6985), 821–827, doi:10.1038/nature02403.

Wullschleger, S. D. (1993), Biochemical limitations to carbon assimilation in C3 plants—A retrospective analysis of the A/Ci curves from 109 species, *J. Exp. Bot.*, *44*(5), 907–920, doi:10.1093/jxb/44.5.907.

Xiao, J., et al. (2010), A continuous measure of gross primary production for the conterminous United States derived from MODIS and AmeriFlux data, *Remote Sens. Environ.*, *114*, 576–591, doi:10.1016/j.rse.2009.10.013.

Xu, L. K., and D. D. Baldocchi (2003), Seasonal trends in photosynthetic parameters and stomatal conductance of blue oak (Quercus douglasii) under prolonged summer drought and high temperature, *Tree Physiol.*, *23*(13), 865–877.

Xu, L., and D. D. Baldocchi (2004), Seasonal variation in carbon dioxide exchange over a Mediterranean annual grassland in California, *Agric. For. Meteorol.*, *123*(1–2), 79–96, doi:10.1016/j.agrformet.2003.10.004.

Yuan, W. P., et al. (2010), Global estimates of evapotranspiration and gross primary production based on MODIS and global meteorology data, *Remote Sens. Environ.*, *114*(7), 1416–1431, doi:10.1016/j.rse.2010.01.022.

Zhang, K., J. S. Kimball, R. R. Nemani, and S. W. Running (2010), A continuous satellite-derived global record of land surface evapotranspiration from 1983 to 2006, *Water Resour. Res.*, *46*, W09522, doi:10.1029/2009WR008800.

Zhao, M. S., F. A. Heinsch, R. R. Nemani, and S. W. Running (2005), Improvements of the MODIS terrestrial gross and net primary production global data set, *Remote Sens. Environ.*, *95*(2), 164–176, doi:10.1016/j.rse.2004.12.011.

Zhao, M., S. W. Running, and R. R. Nemani (2006), Sensitivity of Moderate Resolution Imaging Spectroradiometer (MODIS) terrestrial primary production to the accuracy of meteorological reanalyses, *J. Geophys. Res.*, *111*, G01002, doi:10.1029/2004JG000004.

D. D. Baldocchi and H. Kobayashi, Department of Environmental Science, Policy and Management, University of California, Berkeley, CA 94720, USA.

J. Beringer, School of Geography and Environmental Science, Monash University, Melbourne, Vic 3800, Australia.

T. A. Black, Faculty of Land and Food Systems, University of British Columbia, Vancouver, BC V6T 1Z4, Canada.

A. Knohl, Chair of Bioclimatology, Büsgen Institute, Georg-August University of Göttingen, D-37077 Göttingen, Germany.

B. E. Law, Department of Forest Ecosystems and Society, Oregon State University, Corvallis, OR 97331, USA.

J. Li, Department of Computer Science, University of Virginia, Charlottesville, VA 22904, USA.

O. Roupsard, CIRAD, UMR Ecologie Fonctionnelle and Biogéochimie des Sols and Agroécosystèmes, SupAgro-CIRAD-INRA-IRD, 2 Place Viala, F-34060 Montpellier, France.

Y. Ryu, Department of Landscape Architecture and Rural Systems Engineering, Seoul National University, Seoul 151-921, South Korea. (yryu@snu.ac.kr)

E. van Gorsel, CSIRO Marine and Atmospheric Research, Canberra, ACT 2601, Australia.

C. van Ingen, eScience Group, Microsoft Research, San Francisco, CA 94105, USA.